Reevaluating sedimentary signatures of micro-tidal processes in fluvial-dominated rivers: the Po River (Italy)

Van Yperen, A.E., Finotello, A., Maitan, R., Midtkandal, I., Tognin, D., Ghinassi, M.

Reevaluating sedimentary signatures of micro-tidal processes in fluvial-dominated rivers: the Po River (Italy)

Anna E. van Yperen[1], Alvise Finotello[2], Riccardo Maitan[2], Ivar Midtkandal[1], Davide Tognin[2], Massimiliano Ghinassi[2]

[1]Department of. Geosciences, University of Oslo, Sem Sælands vei 1, 0371 Oslo, Norway.

[2]Department of. Geosciences, University of Padua 35122 Padua, Italy.

Corresponding authors: annavanyperen@gmail.com; massimiliano.ghinassi@unipd.it

---

Abstract

In microtidally influenced rivers, tides are generally assumed to leave virtually no signatures in the sedimentary record. However, this hypothesis has been surprisingly poorly tested using modern river analogues, which provide an opportunity to assess whether sedimentary signatures of microtidal regimes can develop in rivers that lack diagnostic evidence of tidal control on large-scale channel morphology. This study investigates the relative importance of tidal and fluvial processes in shaping sedimentary deposits within the 180-km-long backwater, microtidal fluvial–marine transition zone of the Po River (Italy). The Po River enters the Adriatic Sea through several deltaic distributary channels that exhibit no evidence of funneling or cuspate meanders, indicating a clear morphodynamic dominance of fluvial over tidal processes. Hydrological data show that river water levels are modulated by tidal influence up to ~90 and ~40 km from the river mouth during low- and high-discharge stages, respectively. Approximately 30 km from the mouth, heterolithic deposits formed by riverine floods exhibit clear tidal signatures, including double mud drapes (both equal and unequal) and bidirectional ripples. Around 40 km from the mouth, cross-stratified dunes, and unit bars display bundles with cyclic organization—features that are unclear or absent in analogous bedforms farther upstream. Tidal control of river water levels during the deposition of bedforms with cyclic bundles suggests a linkage to semi-diurnal tidal modulation. These bundles are deposited above the average intertidal zone, indicating that flood-enhanced water levels enable tide-modulated sedimentation to extend beyond the typical intertidal range. This study shows that evidence of tidal processes can be common even in deposits of microtidally influenced rivers, highlighting that tidal signatures may develop where tides exert little to no control on large-scale morphodynamics. Overall, these findings emphasize caution when interpreting dominant morphodynamic processes solely from sedimentary structures—or interpreting structures solely from assumed morphodynamic controls.

6 keywords: microtidal, channel morphology, tidal sedimentary features, high discharge, modern river-delta system

1. Introduction

Within the terminal reaches of microtidally influenced river systems, tides can influence large-scale channel morphology, modulate sediment transport, and affect depositional architecture and facies distribution (e.g. De Mowbray & Visser, 1984; Choi *et al.*, 2004; van den Berg *et al.*, 2007; Choi, 2010, 2011; Hughes, 2011; Sisulak & Dashtgard, 2012; Davis, 2012; Goodbred & Saito, 2012; Leonardi *et al.*, 2015; Lanzoni & D'Alpaos, 2015; Hoitink & Jay, 2016; Gugliotta *et al.*, 2017; Nienhuis *et al.*, 2020; Paniagua-Arroyave & Nienhuis, 2024). Depending on the relative strength of river and wave energy, tidal morphosedimentary fingerprints may be recorded at different scales, ranging from facies-scale features (e.g., couplets/double mud drapes) to typically tide-diagnostic morphological elements, such as cuspate meander bends (Hughes, 2011; Finotello *et al.*, 2020) and funneled channels (Lanzoni & D'Alpaos, 2015). Studies of ancient deposits often assume a direct relationship between the abundance of tidal, wave, or river sedimentary structures and the influence of their respective energy sources on morphodynamic processes (e.g. Ainsworth *et al.*, 2011; Dashtgard *et al.*, 2012; Vakarelov & Bruce Ainsworth, 2013; Rossi *et al.*, 2017). A debated aspect of this approach, particularly when applied to tidal processes, is the general risk of overinterpreting the role of tides based solely on the occurrence of tidal signatures signatures (Gugliotta *et al.*, 2023). This potential overinterpretation of tidal energy in ancient sedimentary successions may conflict with the widely accepted view that tides in microtidal regimes—globally the most prevalent (Archer, 2013)—have little to no impact on morphodynamic processes and leave no clear signature in the sedimentary record (Davis, 2012; Longhitano *et al.*, 2012).

In microtidal regimes, river channels are typically shaped primarily by riverine flows, with tidal energy exerting negligible influence on their morphodynamics (Dalrymple & Choi, 2007; Goodbred & Saito, 2012; Broaddus *et al.*, 2022; Vulis *et al.*, 2023; Paniagua-Arroyave & Nienhuis, 2024). However, recent numerical and field studies have shown that even small-amplitude tides can influence the hydrodynamics and morphology of distributary channels in microtidally influenced river deltas (Sassi *et al.*, 2011; Maselli *et al.*, 2020; Ragno *et al.*, 2020). For instance, Leonardi et al. (2015) show that microtidal oscillations can significantly impact current velocity under both low and high river flow regimes. Additionally, small tidal fluctuations reduce asymmetries in water and sediment fluxes and stabilize channel bifurcations, thereby keeping multiple downstream branches morphodynamically active (Ragno *et al.*, 2020). Despite several studies on the role of microtides in shaping coastal river morphology, limited knowledge remains about their ability to leave discernible imprints on channel deposits. Specifically, it remains unclear whether there is any correspondence between tidal range and the extent of tidal signatures in the stratigraphic record, and whether microtides—despite seemingly having too little energy to shape typical tide-controlled morphosedimentary features—can still leave a detectable signature in the sedimentary record.

Modern river systems serve as natural laboratories, providing the opportunity to directly identify tidal signatures in the sedimentary record and link their distribution to river discharge data. The present work focuses on the distalmost 180 river km of the Po River (Italy), which debouches into the Adriatic Sea under the influence of a microtidal regime (*ca* 1 m). The specific goals of this study are: (i) to test the capability of tidal energy to leave a recognizable signature on channel deposits within a microtidal regime; (ii) to combine discharge data demonstrating the landward propagation of tides under varying river discharge conditions and integrate these findings with down-dip changes in facies, grain size, and cross-stratification characteristics; (iii) to discuss the occurrence of tidal sedimentary features in comparison to morphometric features diagnostic of tidal energy; and (iv) to explore the implications of these findings for the interpretation of ancient deposits.

2. Geomorphological setting

2.1 The Po River

The Po River is a major Italian river, both by length (approximately 690 km) and by drainage area (catchment size ~71,000 km²). The Po River originates in the western Alps and is fed by numerous tributaries from both the Alps and the Apennines. The river ultimately debouches into the northern Adriatic Sea, where it forms an extensive deltaic system (Fig. 1A, B). Alluvial sediment consists of igneous and metamorphic rocks from the Alps and sedimentary rocks from the Apennines (Govi & Maraga, 2005). The river planform configuration is straight-sinuous, with locally well-developed meanders (Fig. 1B) and a few anabranching zones with vegetated mid-channel bars (refs in Lanzoni *et al.,* 2015). The continuity of the main river corridor is interrupted approximately 300 km upstream of the mouth by the Isola Serafini Dam, which was built in 1962 for hydroelectric power production. Continuous riverbank protection and localized groynes control the present-day dynamics of the Po River. A levee system, completed during the 1960s, extends along the final 420 km of the river, including the lower stretches of its tributaries (Govi & Maraga, 2005). The backwater length (*sensu* Paola & Mohrig, 1996) is estimated to be approximately 110 river kilometers (https://www.agenziapo.it/ Fig. 1B, 2A), based on the thalweg channel bed's intersection with sea level (Wright & Parker, 2005; Nittrouer *et al.*, 2011a; Blum *et al.*, 2013; Fernandes *et al.*, 2016; Van Yperen *et al.*, 2024). Discharge conditions are best represented by the Pontelagoscuro gauge station (Fig. 1B) as the flow rate measured there reflects the total flow near the delta apex, before it is partitioned among the main delta distributaries. The Po River annual hydrographs show discharge peaks in autumn

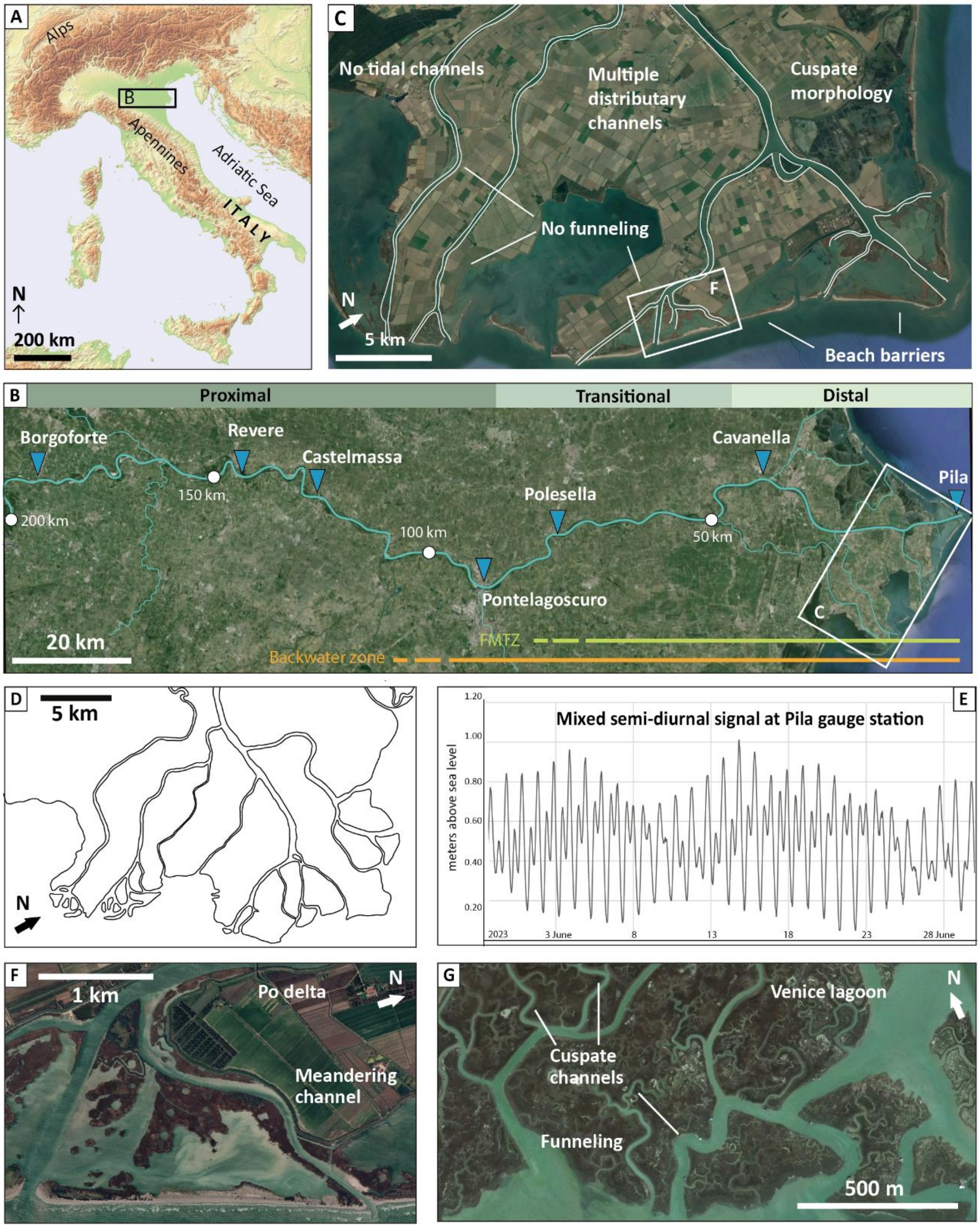

Fig. 1. A) Map of Italy and inset showing location of study area. B) Aerial picture of the studied Po River transect showing gauge locations (blue triangles) and extent of the FMTZ and backwater zone. C) Detailed aerial picture of the Po Delta plain, showing multiple distributary channels and beach barrier ridges, typical for strong influence of river and wave energy, respectively. No morpho-sedimentary features typical for tidal sedimentary processes are present, which is also visible in D) Historical map from 1811 (modified from Visentini & Borghi, 1938). E) Tidal forcing is mixed semidiurnal (data from http://idrometri.agenziapo.it/). F and G: aerial pictures (image©: Google, Landsat/Copernicus) highlighting the contrasting morphological characteristics of the Po River and Venice Lagoon, despite them being only ~70 km apart and experiencing the same tidal forcing.

106 and spring, caused by increased precipitation in autumn and a combination of snowmelt and

precipitation in spring (Milligan *et al.*, 2007). The average discharge of the river is about 1500 m^3/s, with maximum peak discharges around 10,000 m^3/s (Boldrin *et al.*, 2005), albeit that such maximum values are rare. In the last two decades, six episodes of drought occurred, which were characterized by a flow rate (measured at Pontelagoscuro gauge station) lower than 450 m^3/s, of which the most recent occurred in summer 2022 with a negative record of 104 m^3/s (Tarolli *et al.*, 2023). At Pontelagoscuro, the average suspended sediment concentration is 336 mg/L (Nelson, 1970). During river floods, suspended sediment concentrations vary widely, ranging from 940 mg/L (Davide *et al.*, 2003) up to 3,100–4,350 mg/L (Nelson, 1970). The average annual sediment load is estimated at 11.5 $\times 10^6$ tons per year (Correggiari *et al.*, 2005).

2.2 The Po River Delta and tides of the Adriatic Sea

The Po River Delta is one of the largest deltas in the Mediterranean Sea, covering an area of approximately 380 km^2 (Correggiari *et al.*, 2005). The Po Delta progrades into the Northern Adriatic Sea and represents the main component of the late Holocene highstand systems tract that formed after the present sea level highstand was attained (Trincardi *et al.*, 1996; Cattaneo *et al.*, 2003). The Po delta has five main distributary channels feeding discrete lobes, of which the *Po di Pila* has been dominant since the end of the Little Ice Age (Visentini & Borghi, 1938; Nelson, 1970). The modern Po Delta system was deposited during the last *ca* 500 yr, under the impact of short-term climate change, delta lobe switching, and anthropogenic interventions (Correggiari *et al.*, 2005; Trincardi *et al.*, 2019). The Po Delta is a fluvially-dominated, wave-influenced, and tide-modulated system (Fig. 1C), often depicted with a negligible tide-influence on the tripartite Galloway diagram (Galloway, 1975; Bhattacharya & Giosan, 2003; Patruno *et al.*, 2015) or positioned near the center of the diagram (Nienhuis *et al.*, 2020; Vulis *et al.*, 2023). Morphologically, the delta is characterized by a cuspate shoreline and multiple distributary channels, which range from approximately 40 to 500 meters in width and vary from straight to slightly meandering in planform. None of these channels exhibit a funnel-shaped geometry and none of the associated bends display a cuspate morphology. These characteristics are evident in both the current landscape (Fig. 1G, F) and historical maps dating back to 1811 (Fig. 1D) when the delta was even less impacted by human modifications, indicating a negligible contribution of tidal currents to the morphodynamic processes occurring in the distributary channel network.

Tidal forcing in the Northern Adriatic Sea is mixed semidiurnal, with a maximum spring tidal range of ~1 m (Ferrarin *et al.*, 2017) (Fig. 1E). The Northern Adriatic Sea displays unimodal seches of 21.2 h and bimodal seches of 11 h. The dominant winds in the Po Delta area are the south-easterly Sirocco wind and north-easterly Bora wind (Orlić *et al.*, 1994). Under Bora and Sirocco winds, wave heights can reach up to 3 m (Pomaro *et al.*, 2018), occasionally reaching values of ~9 m as the result of storm surges forced by Sirocco wind (Cavaleri, 2000). The combination of meteorological conditions associated with the Sirocco wind and astronomical tides can lead to significant storm surges and prolonged high-water levels, impacting sediment transport and morphology along the Po Delta coastline.

2.3 Study reach and upstream propagation of tides

This study focuses on the final 180 km of the Po River (Fig. 2A), which we divided into three zones, namely proximal, transitional, and distal zones, based on the degree of tidal influence on river water levels under different discharge regimes. This is based on water level data from seven gauge stations distributed along the studied river reach (Fig. 1B), recorded from 2010 to 2022, obtained from the Agenzia Interregionale per il Fiume Po (AIPo; http://idrometri.agenziapo.it/), and referenced to the Italian national vertical datum. In the proximal zone, no tidal-induced changes in water level occur. In the transitional zone, tides are unable to modulate river water levels during high-discharge events. In contrast, in the distal zone, tides are capable of modulating river water levels even during high-discharge events. Following these criteria, the proximal, transitional, and distal zones are positioned upstream of ~90 river km, between ~90 – 40 river km, and from ~40 river km to the river mouth,

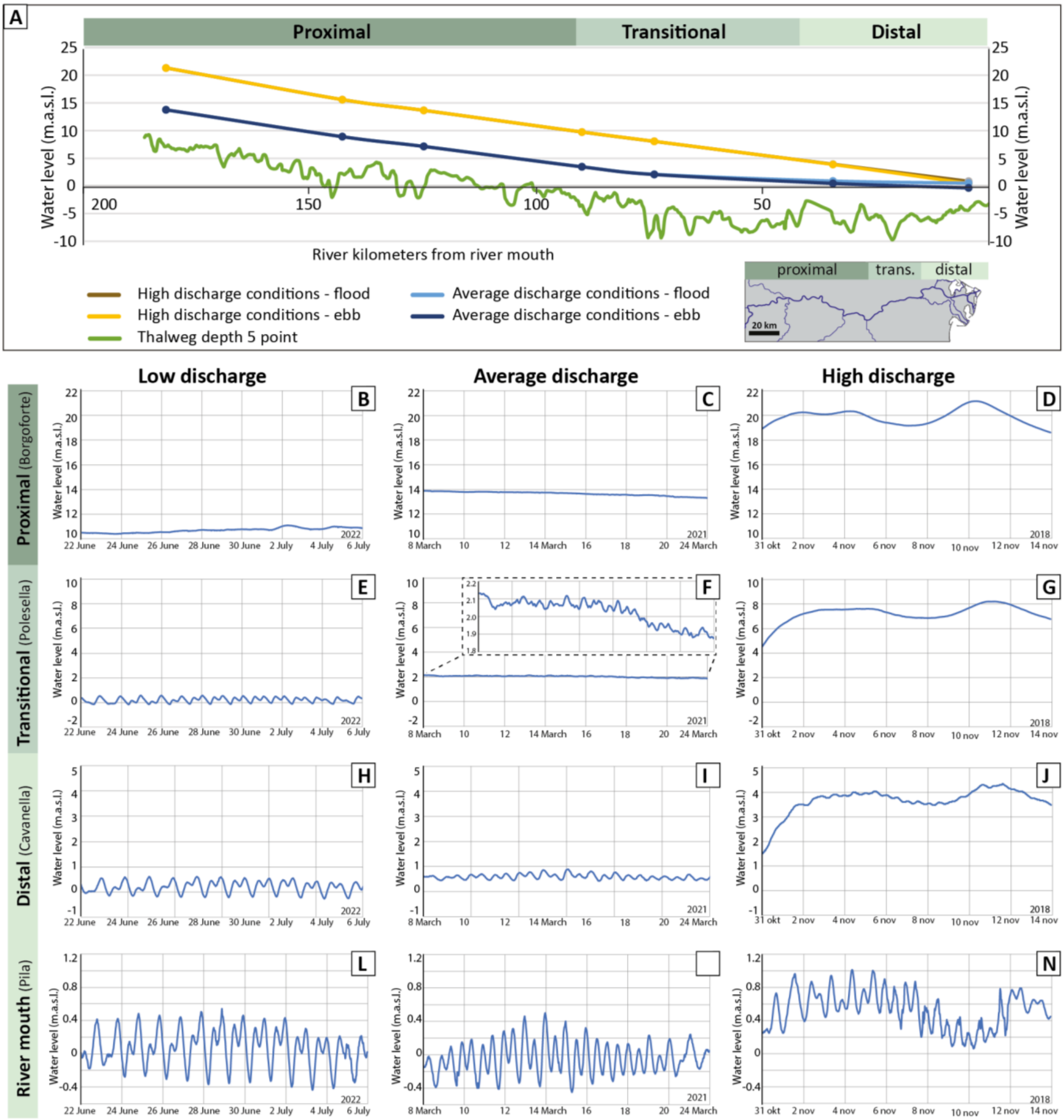

Fig. 2. A) Longitudinal riverbed profile of the 180-km long studied Po River transect along the Pila distributary channel. Water elevation profiles for high and average discharge conditions are shown as well as the channel thalweg elevation. C-M) Water level fluctuations for selected periods representative for low, average, and high discharge conditions.

respectively (Fig. 2A). The upstream limit of the transitional zone (i.e. ~90 river km) parallels the landward extent of the fluvial marine transition zone (FMTZ), which is defined as the landward limit of tidal influence (Dalrymple & Choi, 2007; van den Berg *et al.*, 2007; Martinius & Gowland, 2011; Gugliotta *et al.*, 2016a).

Low, average, and high discharge regimes are distinguished by their characteristic water level patterns (Fig. 2). During low and average discharge conditions, the hydrograph is relatively flat, allowing tidal water level fluctuations in the transitional and distal zones, but tidal amplitudes are generally ~10–30 centimetres larger during low discharge than during average discharge conditions (Fig. 2B, D, E, G, H, I, L, M). At the up-dip limit of the transitional zone (i.e. gauge station Pontelagoscuro), a daily water level fluctuation of approximately 0.05 meters is recorded. During high discharge conditions (e.g. November 2018), water levels rise by several meters near the river apex (i.e., at the Pontelagoscuro gauge station). This dampens tidal fluctuations in the transitional zone (Fig. 2G) and tide-induced water level fluctuations are only recorded in the distal zone (Fig. 2D, G, J, N). Short-lived, minor flood events (< 14 days) reach similar water elevation levels and show little to no tidal modulation in both the distal and transitional zones, respectively (Fig. 3), similar to longer-duration high-discharge conditions.

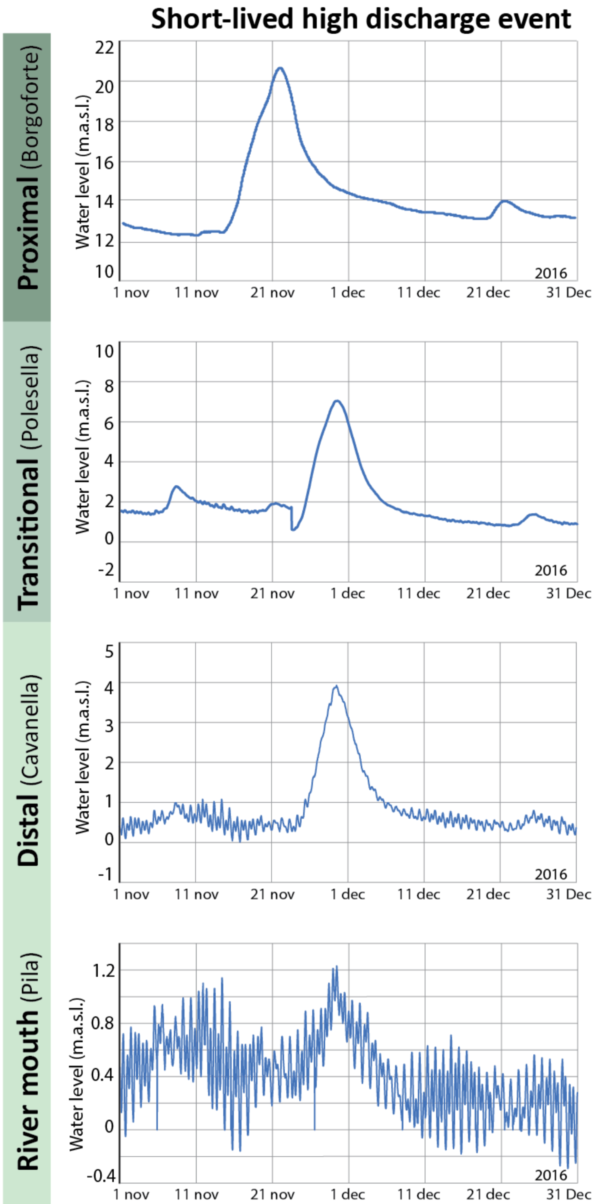

Fig. 3. Water level fluctuations for a short-lived high-discharge event. Vertical axes have same scales as in Figure 2 to allow for comparison. Note how tidal modulation is present in the distal zone (Cavanella) but completely damped in the transitional zone (Polesella).

3. Methods

This study is based on six field surveys conducted between 2022 and 2024, all under fair weather conditions, along the main branch of the Po River, encompassing the proximal, transitional, and distal zones defined in paragraph 2.3 (Fig. 2). During these surveys, we retrieved sediment cores, sampled bars for grainsize, and cut trenches across sand dunes and unit bars to verify cyclicity of cross-stratified deposits.

For grain size analysis, 19 sites in natural bank-attached channel bars were identified with an along-river spacing of 7-10 km (Fig. 4A). At each site, 5 samples were taken spaced 75-100 m apart (Fig. 4B), by recovering a 50 cm long core with a 4 cm diameter. Therefore, a total of 95 samples were taken. All

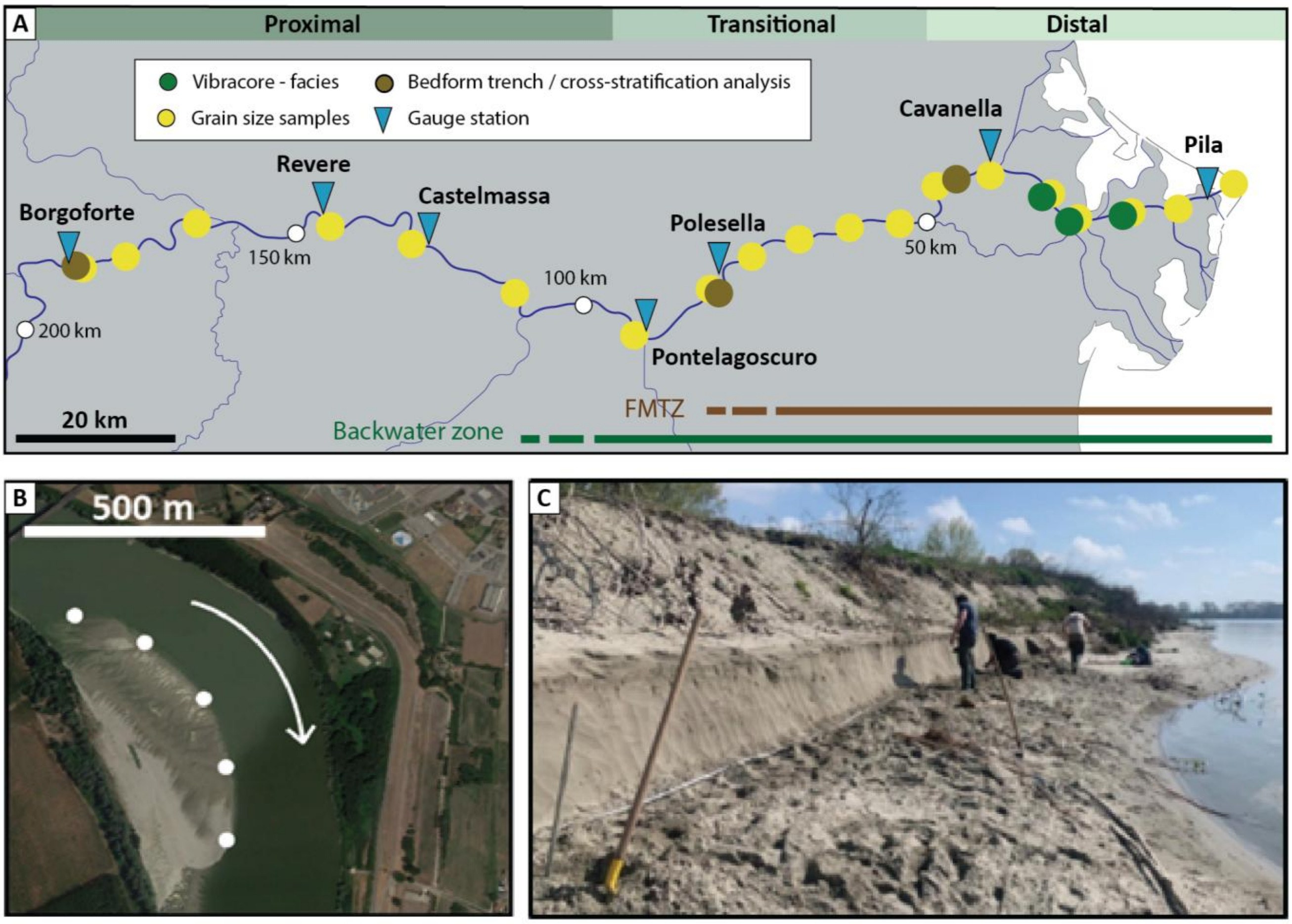

Fig. 4. A) Studied Po River transect with location of data collection; vibracores, grain size samples, trenches for cross-stratification analysis and gauge stations providing historical water level records. Note the identified proximal, transitional and distal zones. B) Each grain-size sample location represents 5 samples taken from channel bars with a ~100-m spacing. Image©: Google, Landsat/Copernicus. C) Example of one of the trenches dug for cross-stratification analysis.

cores were recovered during a phase of low river discharge, during the drought of summer 2022. In the proximal zone, cores were recovered at topographic elevations corresponding to the water level, whereas in the transitional and distal zones, they were recovered from the upper limit of the intertidal zone. Cored deposits were amalgamated, and three replicate subsamples were taken. The grain size was measured using a Mastersizer 2000 (version 5.40; Malvern Instruments, UK). Results were averaged over study sites.

Five vibracores were obtained in the distal ~30 kilometres, as no trenches could be retrieved here due to the permanently high-water table. These cores were taken from the apex of a bank-attached bar and the bar tail of a mid-channel river bar (Fig. 4A), at an elevation corresponding to the upper intertidal level at low-flow conditions (-0.20 to +0.15 m.a.s.l.). The cores are 8 cm in diameter and range from 50 to 230 cm in length. Their orientation relative to the local river flow was recorded. After being split lengthwise parallel to the flow direction, the cores were consolidated with epoxy resin to preserve and highlight internal sedimentary structures.

At three key locations, a total of ten trenches were excavated, covering the proximal (n = 3; Trenches P1 to P3), transitional (n = 5; Trenches T1 to T5) and distal zones (n = 2; Trenches D1 and D2) of the studied reach (Fig. 4A, C). The trenches were 3 to 24.5 m long and exposed cross-stratified sand generated by downstream migration of dunes and unit bars in sections parallel to the flow. All trench sidewalls were photographed, and orthorectified models were produced using Agisoft Metashape Pro®. Where cross sets were fully preserved (e.g. where dune morphology was visible on the trench top), the cross set thickness, or dune height (h_d) was scaled to formative flow depth (H) using Bradley & Venditti's (2017) scaling relationship:

$$H = 6.7h_d \tag{1}$$

Formative depth was not reconstructed for unit bars since they do not scale with water depth (e.g., Herbert *et al.*, 2020). At each trench site, the elevation of the deposits relative to the actual water level was recorded using a Jacob staff, which implies an estimated error of ± 10 cm. The thickness of laminae bundles occurring in the stratified sand of the trench sites was measured in the field (proximal and transitional zone) or extracted from orthomosaic (distal zone). The grain size of dark and light laminae forming different bundles was characterized for a total of 30 lamina-sized samples boy in the proximal and distal zones.

Wavelet analysis was performed to all trench data (n = 10) to examine the possible periodicity and variability of lamina thickness across the deposits, and to evaluate the presence of cyclic organization within strata bundles across the proximal, transitional and distal zones.

4. Results

4.1 Grain size – downdip trend

4.1.1 Description

The median grain size (D_{50}) ranges from 401 to 529 µm (medium sand) between ~90 and 180 kilometres from the river mouth (Fig. 5) which corresponds to the proximal zone. At the landward limit of the transitional zone and the fluvial-marine transition zone (FMTZ), the medium grain size decreases to 26–69 µm (coarse silt) in the segment ~8 to 21 kilometres from the mouth. At the river mouth, the median grain size represents medium grain size values.

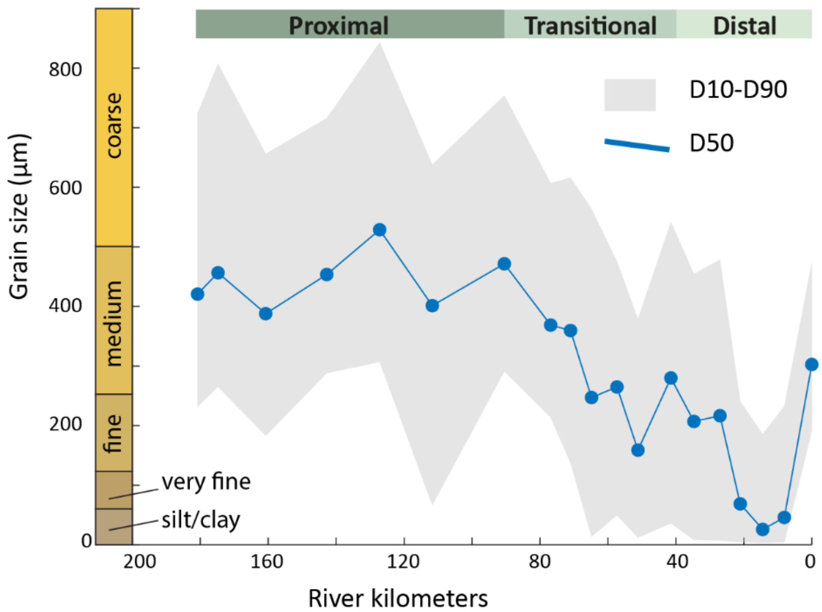

Fig. 5. Grain-size trend along the most downstream ~180 river kilometres of the Po River. Blue dots represent the median grain size fraction at sampled locations, the grey area represents the 10-90 percentile. Each dot represents the average of 5 samples taken from channel bars with a ~100-m spacing.

4.1.2 Interpretation

The simultaneous occurrence of the landward limit of the FMTZ and the onset of seaward-decreasing grain size can be explained by a transition from predominantly bedload deposition controlled by fluvial processes to an increasing influence of suspended load deposition driven by tidal energy in the distal zone. However, similar data for tide-influenced river deltas are rare, and the few available studies show varying relationships. For example, the onset of seaward-decreasing grain size occurs at approximately 680 km in the Mississippi River, which contrasts with a fluvial-marine transition zone (FMTZ) extending only about 280 km (Nittrouer *et al.*, 2011a). In the Mekong River, the grain size begins to decrease landward at around 100 river km, while tidal processes extend up to approximately 395 river km (Gugliotta *et al.*, 2017). The location of the minimum grain size corresponds to the turbidity maximum, matching the location previously reported by Nelson (1970). The subsequent increase in grain size to 302 µm at the river mouth reflects sand deposition transported longshore from the barrier islands.

4.2 Sedimentary facies of the distal zone

Sedimentary cores were recovered from the distal zone, where a minimum of median grain size highlights the occurrence of the turbidity maximum (Fig. 5), and, accordingly, they mainly consist of a mixture of sand and mud deposits (Figs. 6, 7).

4.2.1 Description

Cores from bank-attached deposits sited at *ca* 16 km from the river mouth consist of an alternation between sandy and muddy beds ranging in thickness between 1–20 cm (Fig. 6). These cores recovered sediments until a dept of *ca* 2.5 m at a site where the channel is *ca* 4 m deep, indicating that at least the middle-upper part of the bank-attached bar is made of heterolithic deposits. Sandy beds, 3–20 cm thick, consists of medium to very fine sand. The basal boundary can be either gradational (Fig. 6B) or erosive (Fig. 6C) from mud deposits, whereas the upper boundary is generally transitional into laminated mud (Fig. 6C). These sandy beds mainly show ripple-cross laminations and subordinated plane-parallel laminations, and that are commonly disrupted by dewatering or bioturbation (Fig. 6D). Cross-stratified sand and structureless sand is rare. Mud clasts, 0.5–2 cm thick (Fig. 6E), commonly occur close to the base of sandy layers, whereas plant debris occurs close to their top. Ripple-cross laminated medium to fine sand shows critical to supercritical climbing angles (Fig. 6F) and mainly documents downstream flow direction. Locally, ripples-cross lamination occurring in very fine sand at the top of sandy layers documents an upstream-directed flow (Fig. 6G). Although plane-parallel laminated sandy layers can consist of well-sorted medium-fine sand (Fig. 6B), they mainly occur as poorly sorted medium to very fine sand with mud drapes (Fig. 6H). These drapes, 0.5–1 mm thick, commonly occur as repeated couplets (Fig. 6I), separating 1–3 mm thick fine sand, and consecutive couplets can also repeatedly alternate showing a thick-thin pattern (Fig. 6J). Mud layers are dominantly plane-parallel laminated, but the degree of laminae preservation is highly variable and ranges from very poor (i.e. almost massive mud) to very well-defined (Fig. 6K). Local subtle changes in grain size within the mud deposits suggest structures similar to mud couplets.

Cores from the mid-channel bar tail were recovered approximately 27 km from the river mouth, recovering about 50–100 cm of sediment down from the surface. The recovered deposits include both sand-dominated (cores B, C, Fig. 7) and heterolithic deposits (cores C, D, E, G, Fig. 7). Sand-rich deposits, 5–20 cm thick with erosive bases, are located near the main channel flow. They consist of ripple-laminated and cross-stratified medium sand, indicating a seaward-directed flow (Fig. 7B, C). Cross strata can be either made of well-sorted sand or alternating sand with 0.3–0.5 cm thick mud strata (Fig. 7C, D). Cores consisting of heterolithic deposits (Fig. 7C, D, E, G) were recovered near the front of a seaward-migrating unit bar. The sandy layers commonly include subangular to rounded, 0.5–5 cm mudclasts (Fig. 7C, E). Ripple-laminated sand and plane parallel-laminated medium to fine sand commonly include mud laminae. These laminae, 0.5-2 mm thick, commonly occur as repeated couplets, separating 1-3 mm thick fine sand layers (Fig. 7C, F). Upstream-directed ripple-scale cross laminae occur in the upper part of mud-rich cross strata (Fig. 7F, H)). Mud layers, 0.5–10 cm thick, range from structureless to plane-parallel laminated. Subtle changes in grain size within the mud deposits suggest structures similar to mud couplets.

4.2.2 Interpretation

For most sandy and muddy deposits recovered from the two coring sites, fluvial energy is the sole depositional controlling factor, and the deposits are interpreted to have accumulated during high and low river discharge stages, respectively. The gradational and sharp basal transitions of the sandy layers indicate progressive deposition during the rising phase of a flood, and removal of deposits at peak discharge, respectively. Accordingly, the gradational upper boundaries of these layers reflect the waning phase of flooding. Erosion and fragmentation of muddy beds during flood events are the origin of mudclasts occurring in sandy beds (Li *et al.*, 2017; Gugliotta *et al.*, 2018). Sedimentary structures of the sandy layers point to tractional transport associated with the development of downstream-migrating bedforms under varying flow conditions, predominantly ripples and dunes (Ohata *et al.*, 2022). Plane-parallel stratification in medium sand is attributed to upper plane bed conditions. Differently, these structures in poorly sorted medium to very fine sand with mud drapes likely formed under weak, pulsating currents and limited sediment supply conditions, which triggered local development of low-relief incipient ripples. Muddy layers represent periods of low river discharge at the flood-waning phase, which allows for mud settling on the riverbed (Martin, 2000; Szupiany *et al.*, 2012; Baas *et al.*, 2016). Laminated mud intervals are interpreted as the result of pulses in mud settling, while structureless mud may have formed either through rapid settling or through bioturbation and amalgamation of laminated mud. Structureless layers formed by fluid mud flows are unlikely, considering the limited sediment concentration documented in the river (i.e. < 1 gr/m^3, Nelson, 1970) versus the required concentrations required for fluid mud formation (i.e. 10 kg/m^3, Kirby & Parker, 1982).

The local signature of tides is interpreted based on the presence of several features, of which some are consistent with the influence of tidal currents and indicate tidal modulation of the main river flow.

The heterolithic nature of the deposits, along with the presence of mud drapes, reflects alternating high and low flow conditions across different timescales. The heterolithic bedding itself can result from seasonal variations in river discharge or discrete flood events, and is therefore not diagnostic of tidal modulation (Thomas *et al.*, 1987; Sisulak & Dashtgard, 2012; Baas *et al.*, 2016; Gugliotta *et al.*, 2016b). Single mud drapes may result from temporary slack-water conditions, probably in the order of hours, associated with a reduction or cessation of river flow. These conditions are consistent with flood tides impeding river discharge, but they can also result from autogenic pulses within a single flood event. The features described above are consistent with the occurrence of tidal processes but, on their own, cannot be considered as diagnostic of it.

Contrastingly, upstream-migrating ripples and mud couplets are considered here robust indicators of tidal currents. Upstream-migrating ripples on top of sandy layers (Fig. 7H) document flow reversal at the final phase of a flood event, when flood tides, possibly boosted by atmospheric forcing, were able to reverse the river flow due to its decreased discharge. Similar conditions also occurred where ripples climb along the lee face of unit bars, reaching the crest zone (Fig. 7F), and therefore excluding their origin as counter-current ripples. Mud couplets are the most recurrent evidence for tidal signature in the cored deposits, especially where consecutive couplets alternate with a thick-thin pattern (Fig. 6J). The latter is considered to be particularly diagnostic (e.g. Choi *et al.*, 2021) since they reflect the unequal semidiurnal tides affecting the northern Adriatic Sea. Consecutive mud laminae without thick-thin pattern may arise either from the temporary development of diurnal patterns or from the lack of record of the minor semidiurnal tide.

Overall, the widespread presence of mud couplets and the localized evidence of flow reversal indicate a clear tidal signature on these river-derived deposits, which is also consistent with the frequent occurrence of single mud drapes in the sandy deposits.

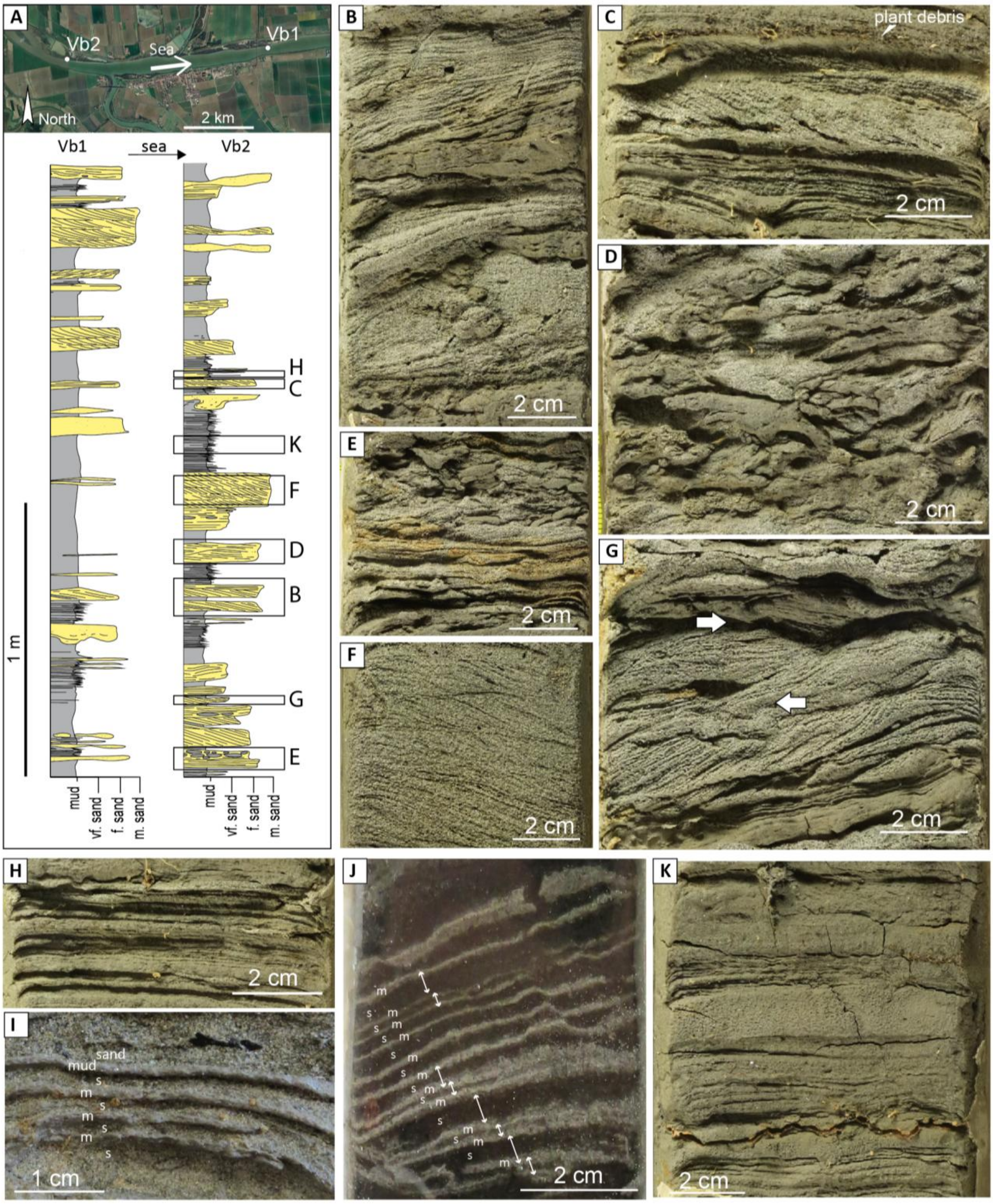

Fig. 6. Photographs of selected facies recovered from the distal zone. A) Location and logs of Vibracore 1 and 2. B) Ripple laminated sand with a gradational lower boundary. C) Mud-sand alternations with erosive basal boundary and transitional upper boundary into laminated mud. D) Dewatering and bioturbation features obliterating original heterolithic bedding. E) Mud clasts. F) Ripple-laminated sand with critical to supercritical climbing angles. G) Upstream-directed ripple-cross laminate at the top of a sandy layer. H). Poorly-sorted medium to very fine plane-parallel laminated sand with mud drapes. I) Consecutive mud-sand couplets. J) Double mud drapes demonstrating a diurnal inequality of semidiurnal tides. K) Plane-parallel mud layers with a varying degree of laminae preservation.

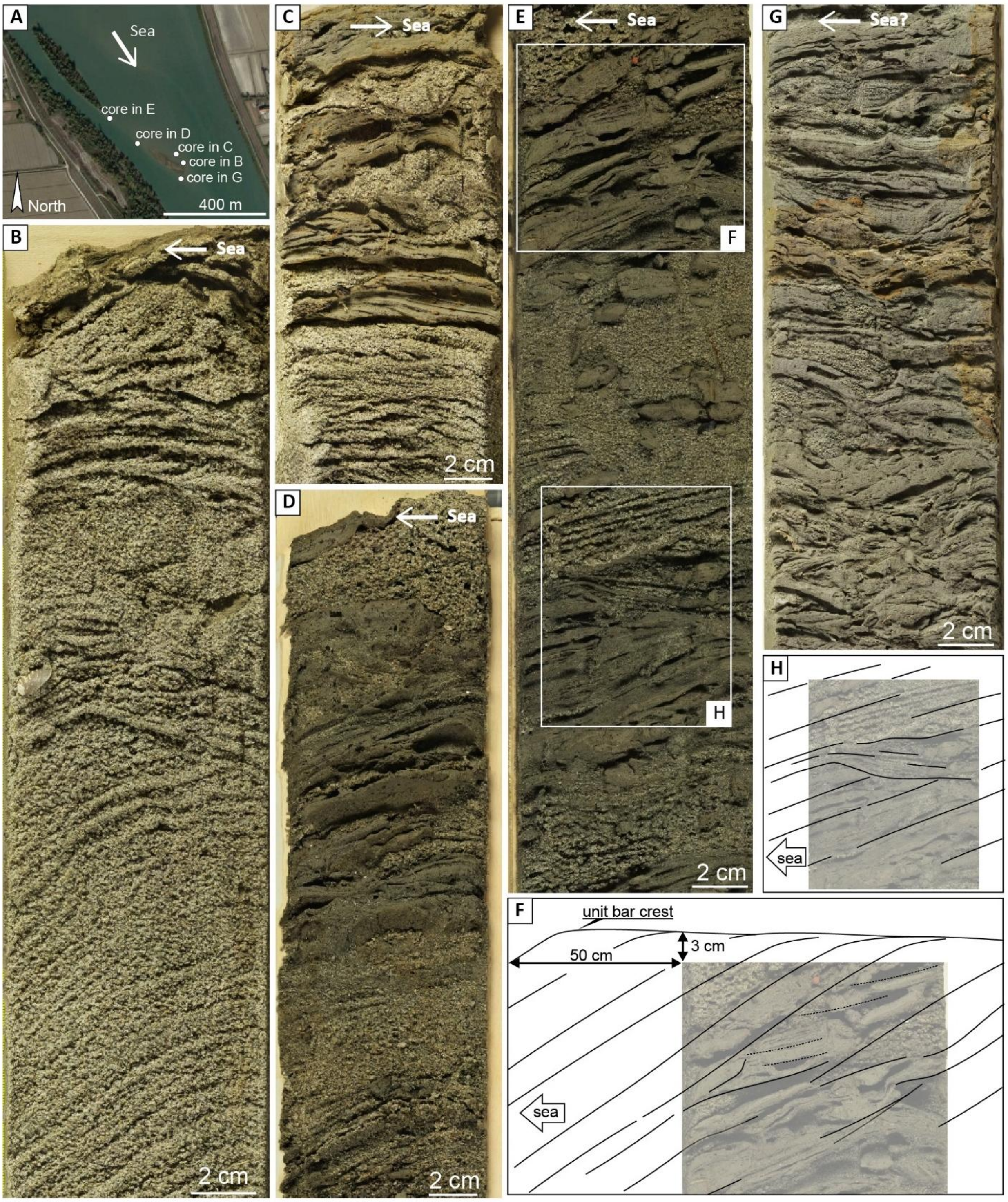

Fig. 7. Photographs of selected facies recovered from the downstream side of a mid-channel river bar in the distal zone. A) Location of the five short cores. B) Seaward directed ripple-laminated and cross-stratified medium sand. C) Well-sorted ripple-laminated sand alternating with mud strata. D) Alternating sand-mud strata. E) Heterolithic bedding with mud clasts and upstream-directed ripple-laminae. F and H) Extrapolation of recovered core based on field on-site observations, highlighting upstream-directed ripple-scale cross laminae in the upper part of mud-rich cross strata. G) Distorted and bioturbated thinly bedded mud-sand alternations.

4.3 Cross-stratified sand and related bundles

4.3.1 Description

Cross-stratified sand exposed in trenches exhibits grain sizes ranging from 1.88 µm (i.e. clay fraction) to 1.43 mm (i.e. very coarse sand), and the thickness of cross-sets varies from 16 to 48 cm. The thickest cross-set occurring at each zone was formed by a unit bar, while all other sets were produced by dunes. The inclined strata dip at approximately 19–30 degrees and are locally defined into light- and dark-coloured bundles, each consisting of multiple foreset laminae with the same characteristics (Fig. 8). The dark-coloured bundles are characterized by well-defined strata ranging predominantly 1–6 cm in thickness (Fig. 8B). Within the light-coloured bundles, stratification is faint and individual laminae/strata have poorly defined boundaries (Fig. 8C). Grain-size analyses reveal that dark strata contain a higher proportion of fine-grained sediments compared to light laminae (Fig. 9). In the upstream reach of the distal zone, two trenches (D1, D2) were dug on the central to downstream reach of the hydrographic right side of a mid-channel bar that accreted between 2013 and 2017 at ~40 km from the river mouth (image: Google, Landsat/Copernicus). Trench D1, measuring 9.37 m in length, exposed cross sets up to 46 cm thick. The local preservation of bedform morphologies and superimposed ripple forms suggests these were generated by migrating dunes (Fig. 10E, F). Trench D2, extending 24.44 m in length, revealed a cross set with a nearly constant thickness of *ca* 50 cm and

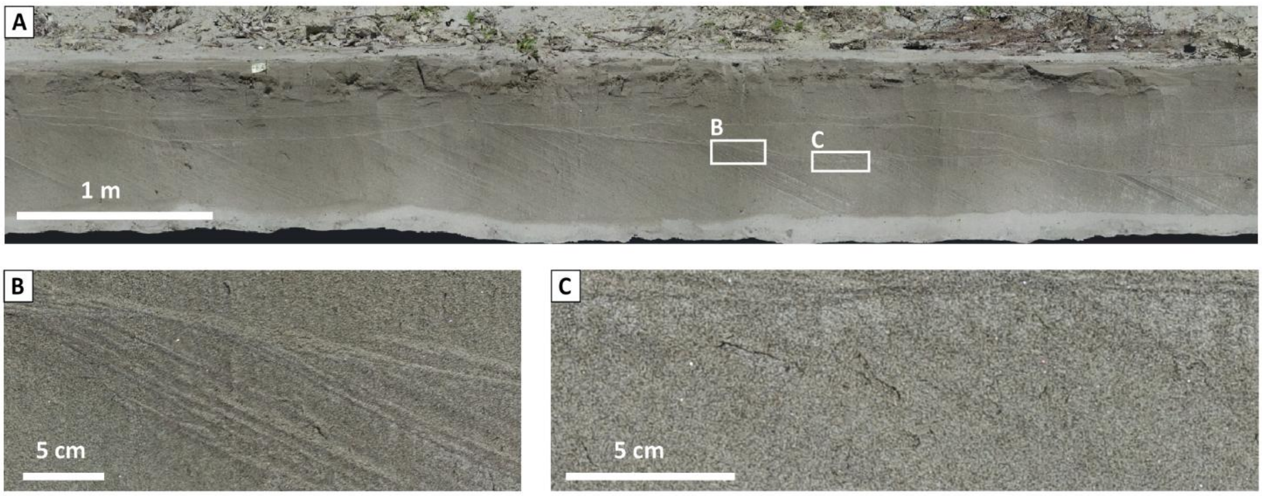

Fig. 8. A) Part of trench T1 from the distal zone, showing alternating dark-coloured bundles with well-defined strata (B) and light-coloured bundles with faint stratification (C).

horizontal top, suggesting it was generated by downstream migration of a unit bar (Fig. 10G, H). Both trenches show no significant changes in strata dip angle. The foreset laminae reveal alternating dark and light strata bundles, with an average lateral extent (one dark and one light bundle combined) of 78 and 86 cm for trenches D1 and D2, respectively. The bundle lateral extent in trench D1 shows a pattern of thickening followed by thinning, while trench D2 exhibits only a thinning pattern (Fig. 10E, G). Cross sets in trench D2 exhibit multiple reactivation surfaces, primarily occurring in two main groups along the downstream extent of the entire cross set. Both sets of reactivation surfaces display an alternation between closely and widely spaced reactivation surfaces. (Fig. 10G-M). Foreset strata are tabular with tangential basal contacts where visible in trench D2, whereas no bottom sets are exposed in trench D1. Spectral analysis using the Continuous Wavelet Transform (CWT) was applied to the cross-set thickness versus space signal (Fig. 11). The resulting Wavelet Power Spectra for both D1 and D2 trenches (Fig 11. A, B) reveal a prominent wavelength band between approximately 65 and 124 cm, which persists consistently along the full length of both trenches. The Global Wavelet Spectrum (GWS) indicates a clear unimodal distribution, with a pronounced spectral peak centred around 78 cm in both cases. While much of the GWS lies just below the 95% confidence threshold, the presence of this peak, hovering near or slightly above the threshold, suggests a potentially meaningful signal, though caution is warranted in its interpretation. Additionally, spectral power is also distributed across shorter wavelengths, hinting at more complex layering patterns at finer scales.

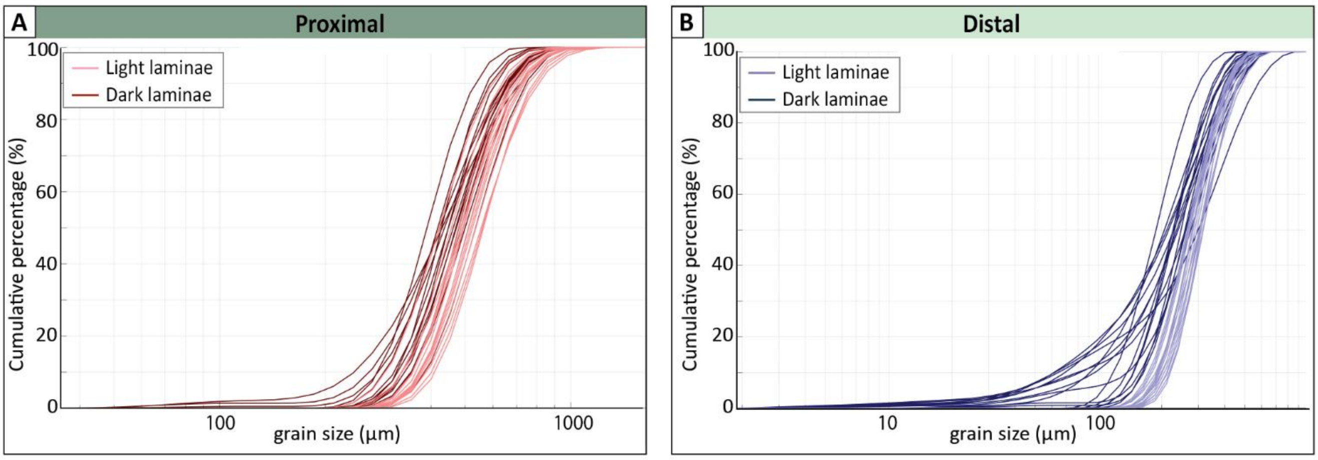

Fig. 9. Cumulative grain size measurements in the proximal and distal zone show clearly an absence and presence of the clay fraction in the light-coloured and dark-coloured laminae, respectively.

In the transitional zone, five trenches (T1–T5) were dug in the central to downstream side of a bank-attached bar situated ~78 km from the river mouth. They range from 3 to 10.8 m in length and expose cross sets ranging in thickness between 16 and 36 cm (Fig.10; Appendix A). Trenches were dug on top of preserved dunes (Trenches T1–T4) and a unit bar (Trench T5). Where visible, foreset laminae are tabular with tangential basal contacts where visible (Trenches T1–T3) (Fig. 10C, D), angular basal contacts (Trench T4), and alternating angular and tangential basal contacts (Trench T5). Reactivation surfaces occur in Trenches T1, T3 and T4 and are randomly distributed rather than having a cyclical pattern. The foreset angles before and after reactivation show no significant changes. Laminae are locally organized into dark and light bundles (with lateral extent ranging from 30 to 130 cm), although this organization is less evident than in the distal zone. Indeed, the Continuous Wavelet Transform (CWT) applied to the cross-set thickness versus space signal (Fig. 11C, D) for both Trench T5 (unit bar) and Trench T4 (dune) does not reveal a clearly dominant wavelength band along the length of either trench. The Global Wavelet Spectrum (GWS) shows that spectral power is mostly concentrated at relatively short wavelengths (less than 16 cm), with no strong or distinct peaks. A possible multimodal pattern emerges at Trench T4, but overall spectral power remains generally below the 95% confidence threshold. This suggests that much of the variability may be due to random fluctuations (i.e. noise), although localized signals that fall just short of statistical significance cannot be ruled out.

In the proximal zone, three trenches (P1–P3) were dug in the central to downstream side of a bank-attached bar sited at ~77 km from the river mouth. They span from 4.6 to 7.8 m in length and were cut on top of preserved dunes (Trench P1 and P2) and a unit bar (Trench P3), which were ubiquitously draped by ripple forms. Exposed cross sets range in thickness between 18 and 26 cm (Fig. 10A, B; Appendix A). Foreset strata are tabular with alternating angular and tangential basal contacts in trench P3 and are not visible in the other trenches. Reactivation surfaces occur in Trench P1 and P3 but show no cyclic pattern. No ‘bundling’ of dark and light laminae is identified. This is quantitatively supported by the Continuous Wavelet Transform (CWT) applied to the cross-set thickness versus space signal (Fig.

11E, F), which indicates a relatively weak spectral structure compared to the distal zone, with no consistent or dominant wavelength bands across the trench length. The Global Wavelet Spectrum (GWS) shows spectral power distributed broadly across wavelengths, with no distinct peaks or strong patterns emerging. Most of the GWS lies below the 95% confidence threshold. However, this does not entirely preclude the possibility of subtle or localized signals that fall just short of statistical significance.

4.3.2 Interpretation

Cross-stratification bundling has been widely associated with tidal processes, occurring in purely tidal environments (Boersma, 1969; Visser, 1980; Terwindt, 1981) or through modulation of unidirectional riverine currents during floods (Martinius & Gowland, 2011; Gugliotta *et al.*, 2016a; Hendershot *et al.*, 2016). Nevertheless, experimental studies show that similar bundling can also result from the migration of superimposed bedforms (Reesink & Bridge, 2007, 2009). These superimposed bedforms temporarily alter sediment sorting on the lee slope of host bedforms, thereby imitating the effects of tidal modulation on the migration of a river-generated bedform (Reesink & Bridge, 2007, 2009). Finally, bundles can also be generated far away from the coastline as a consequence of river discharge pulses that can promote variations in migration dynamics of avalanching fronts (Ainsworth *et al.*, 2012). Based on this, both river discharge and tidal modulation can be discussed as possible mechanisms generating bundles (Fig. 2H, Fig. 10E-H, Fig. 11).

The internal organization of cross-stratified bedforms in the distal zone reveals the cyclic occurrence of bundles, whereas the trenches of the proximal reaches of the study area consistently lack cyclic patterns. In the transitional zone, bundles occur but without consistent cyclic organization. These differences are quantitatively supported by spectral analysis, which reveals a pronounced spectral peak and dominant periodicities in the distal zone. In contrast, the transitional and proximal zones show no significant spectral power peaks, with global wavelet spectra falling below the 95% confidence threshold—indicating that observed variations are likely due to random fluctuations (Fig. 11).

In the distal zone, a tide-modulated origin for the dark-coloured bundles is interpreted based on the following. Note that these bundles differ from 'tidal bundles' (sensu stricto, Boersma, 1969; Visser, 1980), for which tidal energy is the sole depositional controlling factor. The occurrence of consistently spaced dark bundles, which have a higher proportion of fine-grained sediments compared to light laminae, indicates periodic declines in fluvial discharge which facilitated accumulation of fine-grained sediments in foreset strata (Fig. 9). These periodic discharge declines are consistent with the capability of tides to control water level also during major floods (Fig. 2H–J) and align with tidal modulation of the riverine flow, with flood tides reducing river discharge and triggering mud settling at the front of bedforms. The lack of changes in strata dip angle also argues against superimposed bedforms as the primary control on bundle formation (Reesink & Bridge, 2009). The limited percentage of mud in the dark bundles fits with the limited suspended load capability of the Po River (Nelson, 1970) and also with the location of the trench sites at *ca* 15–20 km upstream of the maximum turbidity zone. Further evidence supporting the tidal modulation of these bundles comes from the record of water elevation data between 2013 and 2017, when the studied beds accumulated. These data show that the receding (i.e. depositional) phase of major floods lasted between 0.5 to 9.5 days and that a semi-diurnal modulation of water level occurred also during these events (Fig. 2J). Linking the 12 and 26 bundles observed in the trenches (D1, D2) to semi-diurnal tidal cycles suggests deposition periods of approximately 6 and 13 days, respectively, being consistent with the recorded duration of the flood waning stages. This interpretation would provide an overall migration rate of ~1.5–1.7 m/day for the studied bedforms, a rate that is comparable to the ~1 m/day documented by Trincardi et al. (2019) for dune migration during a flood in the distalmost reach of the Po River. Interpretation of tidal modulation as the primary forcing on the development of bundles in the distal zone does not exclude the superposition of different processes for bundle formation, like riverine pulses or bedform superposition, which may mask a complete record of tidal modulation (Gugliotta *et al.*, 2016a; b).

The bundle lateral extent in trench D1 shows a pattern of thickening followed by thinning, which could reflect neap-spring cyclicity. In trench D2, however, the consistently thinning trend could be explained by the waning energy of the river flood, resulting in diminishing thicknesses. In trench D1, several sets of closely spaced reactivation surfaces are observed (labelled 0, 1, 2 in Fig. 10H, J), though their formation mechanism remains unclear. Based on the interpretation of a semi-diurnal tidal signal and the presence of approximately 13 bundles between these surfaces (including the reactivation surfaces themselves), the intervals between them suggest a separation of about 6–7 days. Commonly, reactivation surfaces are related to either neap tides (due to small time velocity asymmetry and weak current speeds below the threshold of dune existence, Choi & Kim, 2016) or spring tides (subordinate currents strongest during spring, hence most discordance, e.g., De Mowbray & Visser, 1984). However, the bundles in this trench lack a clear thickening or thinning trend typically associated with neap-spring cyclicity, and their positioning (i.e. an interpreted 6-7 days apart) appears problematic as a correlation to either spring or neap would imply ~14 days of deposition between them. In combination with the consistently thinning trend—likely caused by the waning energy of the river flood and resulting in progressively thinner deposits—these reactivation surfaces were probably formed by short-lived discharge variations during high-discharge events, rather than by tidal processes.

In the transitional and proximal zones, the absence of cyclic tidal modulation on bundle formation is evident, as their organization is weak and sparse in the transitional zone, and nearly absent in the proximal zone. This is also quantitatively supported by wavelet analysis that shows no cyclicity nor any spectral power peaks with the least structure in the proximal zone (Fig. 11C–F). This progressive upstream decrease in tidal signature within cross-stratified sand aligns with the diminishing capability of tides to control water levels and modulate river velocities also during high-discharge conditions (Fig. 2G, J), as documented in other systems (Dalrymple *et al.*, 2015; Gugliotta *et al.*, 2017). The limited occurrence of a cyclic signal in the transitional zone would, therefore, reflect the attempts of tides to modulate river discharge during short periods of low river energy. However, most bundling-like features observed in the transitional and proximal zones can be mainly attributed to either superimposed bedforms (Reesink & Bridge, 2007, 2009) or minor fluctuations in river discharge (Ainsworth *et al.*, 2012). Similarly, reactivation surfaces are also interpreted to result from the superposition of dunes migrating at different rates or non-steady flow conditions due to changes in river discharge in purely fluvial conditions (Rubin & Hunter, 1982; De Mowbray & Visser, 1984; Reesink & Bridge, 2009, 2011; Best & Fielding, 2019; Herbert *et al.*, 2020). The occurrence of both angular and tangential bottom sets, although only documented in trench P3 and in rare intervals of trenches T1 – T5, reflects the absence and presence of lee side flow separation, respectively. This can be caused by changes in flow velocity resulting from alternating flood retardation and ebb acceleration (Martinius & Gowland, 2011) or variation in flow rate, bed roughness, and dune crest shape (e.g. Lefebvre & Cisneros, 2023).

4.4 Deposition during high discharge: formative flow depth from cross-stratified dunes

Estimation of formative flow depth from fully preserved dune cross-sets (Bradley & Venditti, 2017) indicate water depths consistent with deposition during high-discharge events across all zones, made exception for some average discharge events in the transitional zone (Table 1). Notably, high discharge events in the distal zone are clearly tide-modulated (Fig. 2J, N and 3). This is reflected in the related deposits, as these reveal consistently spaced bundling indicative of tidal modulation in Trenches D1 and D2 (Fig. 10E–H).

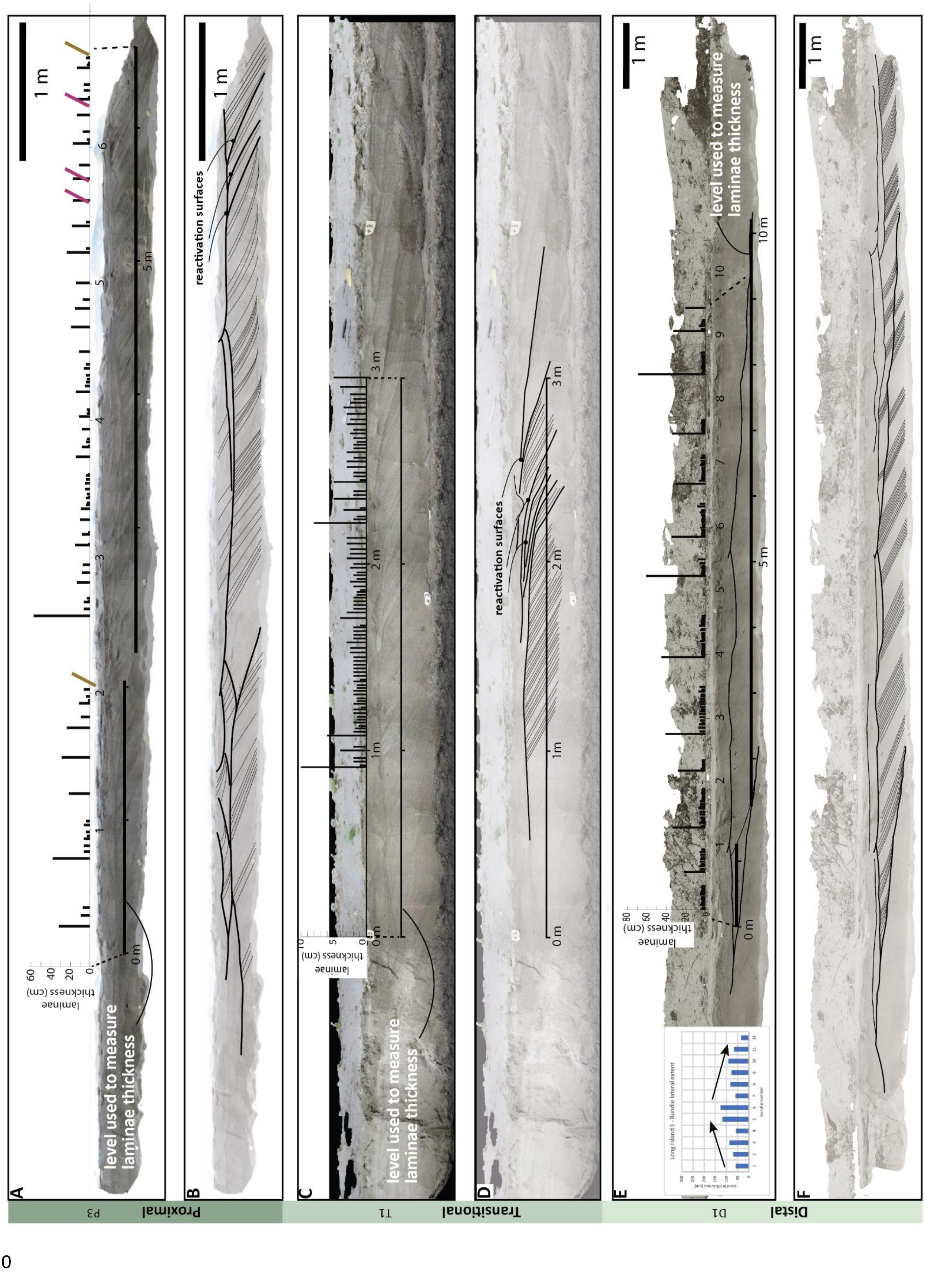

A
level used to measure laminae thickness
laminae thickness (cm)
1 m
0 m
5 m
B
reactivation surfaces
1 m
C
level used to measure laminae thickness
laminae thickness (cm)
0 m
1m
2 m
3 m
D
reactivation surfaces
0 m
1m
2 m
3 m
E
level used to measure laminae thickness
laminae thickness (cm)
1 m
0 m
5 m
10 m
Long Island 1 - Bundle lateral extent
bundle number
F
1 m
Proximal
P3
Transitional
T1
Distal
D1

Fig. 10. (two pages) Orthorectified models for selected trenches from the proximal (A, B), transitional (C, D) and distal (E-J) zone. K-M show close-ups of reactivation surfaces. Note the presence of a cyclic pattern in cross-stratification bundling in the distal zone (E-J), contrasting the lack thereof in the proximal zone (A-B).

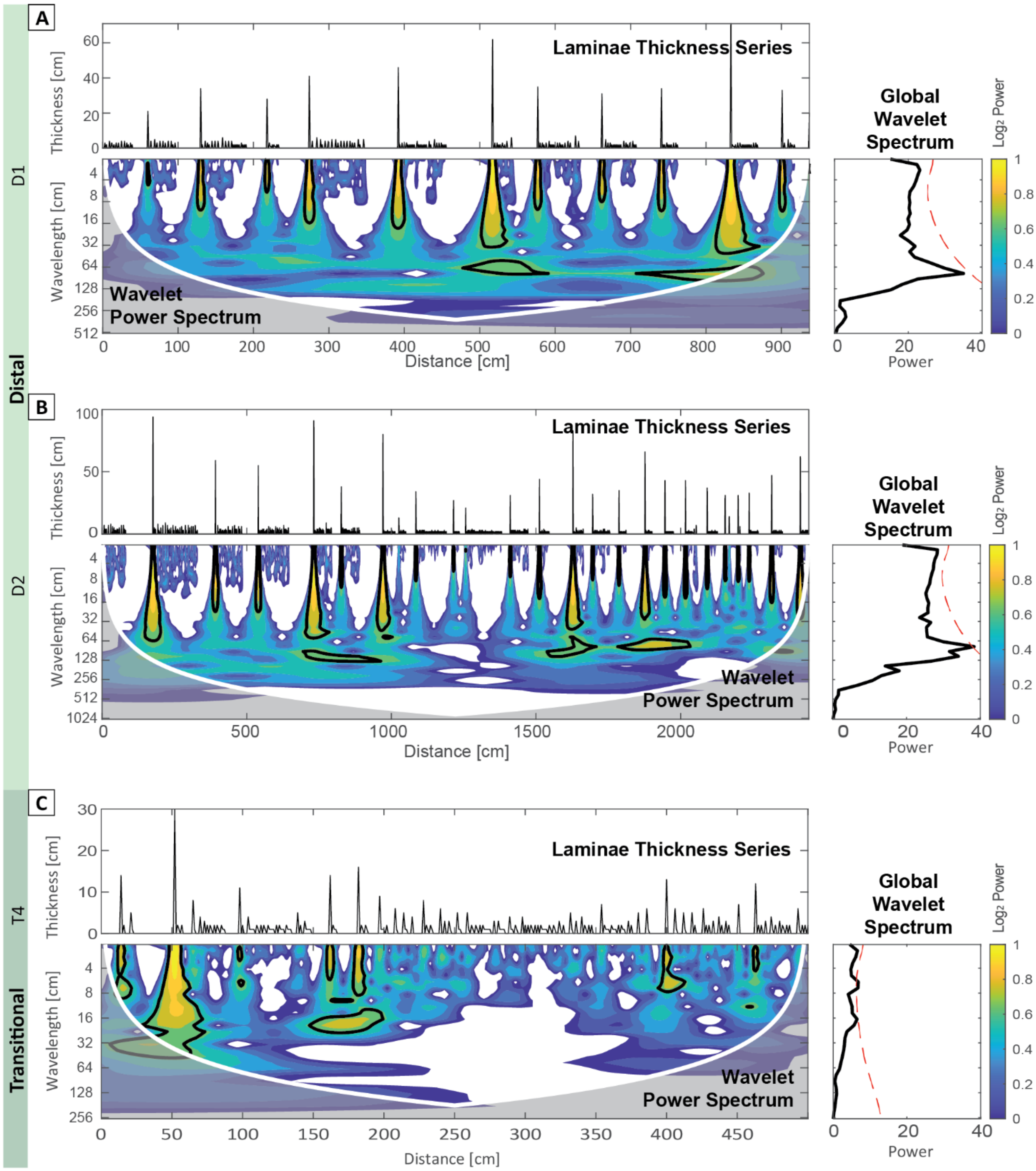

492

Fig. 11. (two pages) Continuous Wavelet Transform (CWT) analysis of selected trenches. For each trench, cross-set thickness is plotted against progressive along-trench distance (top panel). The wavelet Power Spectrum showing the spatial distribution of dominant wavelengths in the cross-set thickness signal; the cone of influence (COI) is indicated by the non-gray-shaded region (lower panel). Thick black contours mark the 95% confidence level relative to a red-noise background spectrum with the same lag-1 autocorrelation as the analyzed signal. For each trench, the Global Wavelet Spectrum (GWS) is displayed on the right-hand side; the dashed red line represents the 95% confidence interval."

493

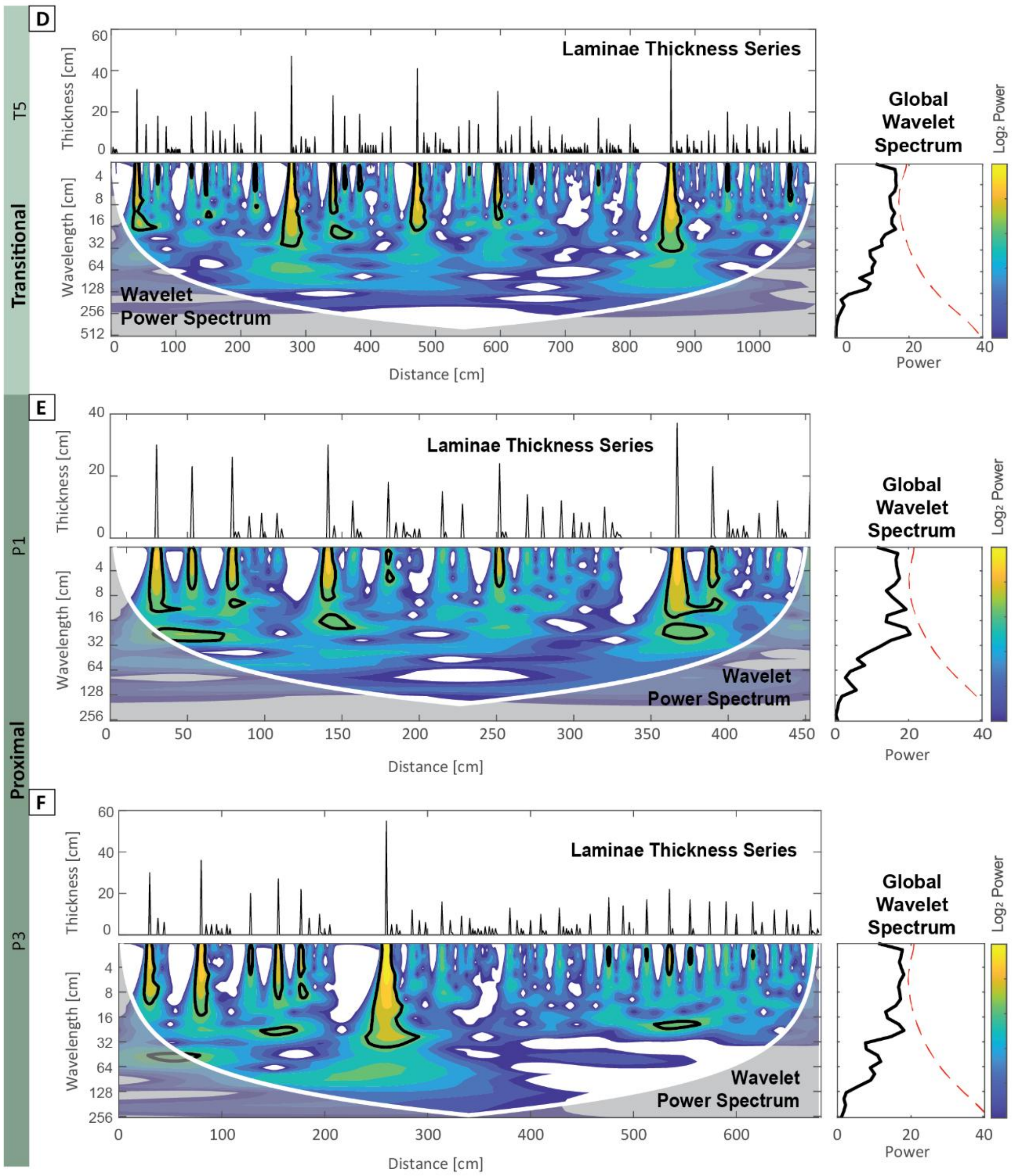

D
Transitional
T5
Laminae Thickness Series
Thickness [cm]
Wavelength [cm]
Wavelet
Power Spectrum
Distance [cm]
Global
Wavelet
Spectrum
Power
Log₂ Power
E
Proximal
P1
Laminae Thickness Series
Thickness [cm]
Wavelength [cm]
Wavelet
Power Spectrum
Distance [cm]
Global
Wavelet
Spectrum
Power
Log₂ Power
F
P3
Laminae Thickness Series
Thickness [cm]
Wavelength [cm]
Wavelet
Power Spectrum
Distance [cm]
Global
Wavelet
Spectrum
Power
Log₂ Power

494

Part of study area	Trench code	Cross-set thickness (m)	Formative flow depth (Bradley & Venditti, 2017)	Water depth at gauge station needed to deposit bedform (m.a.s.l.)	Stage needed for bedform deposition
Proximal zone	P1	0.18	1.21	15.76	high discharge event
Proximal zone	P2	0.19	1.27	15.83	high discharge event
Proximal zone	P3 (unit bar)	0.26	-	-	-
Transitional zone	T1	0.36	2.41	3.42	high discharge event
Transitional zone	T2	0.18	1.21	2.22	average
Transitional zone	T3	0.2	1.34	2.35	average
Transitional zone	T4	0.16	1.07	2.08	average
Transitional zone	T5 (unit bar)	0.34	-	-	-
Distal zone	D1	0.46	3.08	3.08	high discharge event
Distal zone	D2 (unit bar)	0.48	-	-	-

Table 1. Estimated flow depth based on the empirical scaling relationship between dune height and formative flow depth from Bradley & Venditti (2017). The stage needed for bedform deposition results from the waterdepth at gauge station needed to deposit the bedform and its relation discharge values computed / introduced in chapter 2.3. Formative depth was not reconstructed for unit bars, since they do not scale with water depth (in Herbert et al., 2020).

5. Discussion

5.1 Unexpected extent of upstream propagation of microtides

Upstream propagation of microtidal waves within river channels is generally considered negligible, as shown by the Yellow River in China where spring tides, with a range of ~1.1 meters, propagate only about 20 km upstream (Yu *et al.*, 2023). However, this intuitive pattern is contradicted by gauge station data from the Po River, which has a similar spring tidal range of around 0.9 meters and exhibits tidal modulation extending approximately 50 km inland during high discharge, and up to 90 km during low discharge conditions. Even more striking, the Mississippi River (spring tidal range ~0.45 m) shows propagation of tides up to 280 km upstream (Nittrouer *et al.*, 2011a). However, the comparability of these contrasting landward propagation extents may be limited, as the data sources differ: water level fluctuations for the Po and Mississippi rivers are based on gauge station measurements, whereas the upstream extent of tidal influence in the Yellow River is inferred from modelled salinity data (Yu *et al.*, 2023) and observed siltation patterns (Wang & Liang, 2000), due to the absence of gauge stations in its lower reaches. Nevertheless, these examples collectively demonstrate that even relatively small tidal excursions can propagate tens of kilometres upstream along the main river channel.

In general, upstream-propagating tidal waves change in amplitude and shape as a result of a complex interplay between channel narrowing, tidal range, bottom friction, river discharge, riverbed slope, and river depth (e.g. (Dalrymple & Choi, 2007; Dalrymple *et al.*, 2015; Guo *et al.*, 2020). Channel narrowing reduces cross-sectional area, which amplifies tidal waves and increases flow velocity. In contrast, bottom friction dissipates tidal energy, reducing wave amplitude and counteracting the effect of narrowing (Jay, 1991; Savenije *et al.*, 2008). Larger tidal ranges promote greater landward propagation of tides (Nichols & Biggs, 1985; Dykstra *et al.*, 2022). Increased river discharge dampens tidal modulation by raising mean flow velocity and, consequently, friction (e.g. Dalrymple & Choi, 2007; van den Berg *et al.*, 2007). However, recent studies reveal a more complex picture, with simultaneous tidal amplification in seaward reaches and damping in landward reaches (Dykstra *et al.*, 2022) as well as enhanced low-frequency tides during high flows (Guo *et al.*, 2020). A lower riverbed gradient also favours the landward propagation of tides, assuming all other conditions remain constant (Dalrymple *et al.*, 2015; Kästner *et al.*, 2019). Finally, shallow river systems generally exhibit shorter tidal penetration due to increased bottom friction (Godin, 1991; Dalrymple *et al.*, 2015).

No single factor consistently explains the differences in upstream tidal propagation among the selected microtidal rivers, i.e. the Po, Yellow, and Mississippi rivers. For example, there is no significant relationship between tidal range and the landward extent of tidal propagation. Notably, the Mississippi River, with the smallest tidal range (0.45 m), exhibits the greatest landward tidal penetration (280 km) (Table 2). Additionally, the steeper coastal plain gradient of the Po River compared to the Mississippi River corresponds with the latter's greater tidal propagation (Table 2), while the Yellow River exhibits a shorter tidal limit than the Po, despite the Po's somewhat steeper coastal gradient. These examples illustrate that upstream tidal propagation cannot be fully explained by a single factor. Nonetheless, the three rivers support the broader trend that larger rivers flowing over low-gradient coastal plains tend to exhibit longer tidal penetration than smaller rivers with steeper slopes (Dalrymple et al. 2015).

The wide range of influencing factors and their interactions underscores the complexity of upstream tidal propagation and cautions against relying on tidal range alone to predict the landward extent of tidal influence. We argue that the notable upstream propagation of tides in the Po River results from a combination of a low coastal plain gradient, a relatively uniform channel width, and a consistent depth profile over the lowermost ~100 km of the river. Together, these characteristics limit energy dissipations and facilitate the landward transmission of tidal signals.

	Landward limit tidal range (km)	**Spring tidal range (m)**	**Tidal cycle**	**Average discharge (m3/s)**	**Gradient between apex and coastline**	**Intersection river bed with sea level (backwater) (km)**
Po river	90	0.9	semidiurnal	1500	8.00E-05	100
Mississippi River	280	0.5	diurnal	15000	3.88E-05	680
Yellow River	20	1.1	weakly semidiurnal	1550	6.10E-05	14

Table 2. Key characteristics of the river-delta systems discussed in Section 6.1, relevant for comparing upstream tidal propagation. Data sourced from (Boldrin et al., 2005; Nittrouer et al., 2011a; Zheng et al., 2019; Yu et al., 2023).

5.2 Abundant tidal sedimentary features but no tide-controlled planform morphologies

The Po River delta presents and intriguing paradox: despite abundant tidal signatures in its sedimentary deposits, it lacks the characteristics morphology typically associated with tide-dominated systems. In such systems, tides typically shape channels with funnel-shaped planforms and promote channel straightening due to the increasing tidal flux in the seaward direction (Dalrymple & Choi, 2007; Lanzoni & D'Alpaos, 2015). Seaward channel shallowing is also common and is attributed to the landward redistribution and temporary storage of river-supplied sediment by tidal currents (Gugliotta and Saito, 2019). However, large-scale tide-generated morphology in the microtidal Po River delta channels is absent (Fig 1C, D, F), which contrasts the frequent evidence of tidal indicators in the studied deposits. Diagnostic features such as mud couplets and bundles are common up to 30 km from the river mouth, along with other evidence of tidal influence, including flow reversals and mud drapes.

The widespread occurrence of tidal signatures in the Po River indicates that even microtidal conditions can imprint recognizable features in the sedimentary record. This observation aligns with recent studies suggesting that microtides may also contribute to reduced channel mobility (Ragno *et al.*, 2020) and enhance tidal velocity amplitudes at the distributary river mouth (Leonardi *et al.*, 2015). Nevertheless, microtides are unable to impact morphodynamic processes to generate typical tide-controlled morphosedimentary features such as funneling (Lanzoni & D'Alpaos, 2015) and cuspate meander bends (Hughes, 2011). A comparison with the microtidal Mississippi River and the adjacent Wax Lake Delta could provide valuable context to support observations from the Po River. However, sedimentological descriptions of related deposits are limited and primarily note the presence of heterolithic deposits within distributary channels (Coleman & Gagliano, 1960). The interlaminated thin sands, silts, and clays reported for the Wax Lake Delta (Roberts *et al.*, 1997) also lack detailed characterization, though they suggest that the presence of tidal indicators cannot be dismissed. Morphological changes attributable to tidal energy occur in the final 120 kilometres of the river and the main channel widens in the last 30 kilometres (Nittrouer *et al.*, 2011b). This shows that morphosedimentary features typical for tides can be formed in micro-tidal settings, despite their absence in the Po River.

The surprising ability of tides to leave distinctive sedimentary signatures even where they exert little geomorphic influence is counterintuitive and holds significant implications for the interpretation of ancient deposits (see paragraph 5.4). This tendency is likely linked to the substantial effect of tidal oscillations on the transport capacity of riverine flows. Evidence from the Po River shows that flood tides can elevate the water surface and increase the channel's cross-sectional area, leading to a reduction in flow velocity and sediment transport capacity, thereby facilitating the formation of bundles or mud drapes. However, the occurrence of tidal signatures identified through the integration of sedimentological observations and river discharge data does not necessarily reflect to what extent tidal energy influences fluvial processes. For instance, mud couplets formed under tidal modulation (e.g. by river current acceleration and deceleration) in the Po River are practically indistinguishable from those formed in environments where tidal dynamics dominate sedimentation (e.g. current reversal forming couplets). This underscores the absence of diagnostic criteria to differentiate between structures generated directly by tidal currents and those formed by tidal modulation of pre-existing river flows.

This discrepancy between abundant tidal signatures and the absence of tide-dominated morphology in the Po River delta reveals a complex interplay between tidal influence and fluvial processes. It suggests that the presence of tidal indicators in sedimentary deposits may not always correlate with the degree of tidal impact on overall delta morphology, challenging conventional interpretations of ancient deltaic systems in the rock record. This knowledge gap has important implications for stratigraphic interpretation and highlights the need for further research.

5.3 Dynamic intertidal zone – tidal signature in river-flood deposits

High-discharge conditions are known to damp tidal modulation (e.g. Dalrymple *et al.*, 2015; Gugliotta *et al.*, 2017), therefore lowering the chance of tidal signature being recorded. Accordingly, the control of river discharge on inland tidal propagation (e.g., Fig. 1.5 in Dalrymple *et al.*, 2015) and water level elevation in tide-influenced rivers or estuaries (e.g., Hoitink & Jay, 2016; Gugliotta *et al.*, 2017) has been described. Preservation of tidal signature is also controlled by location within the vertical profile of channelized deposits, being the mid-lower part of channels not prone to record tidal processes due to the exceeding high-energy conditions that promote continuous sediment reworking and scarce mud accumulation (Tessier, 1993; Choi *et al.*, 2004; Choi, 2010, 2011; Davis, 2012; Cosma *et al.*, 2022). Within this framework, limited attention has been given to the effects of heightened river discharge on the preservation of tidal signatures, and to the concept that different flood stages cause the vertical position of the ’tidal signature recording zone’ to be dynamic rather than static.

Specifically, high-discharge conditions elevate water levels, enabling tidal modulation to influence areas higher than the typical ‘average-discharge intertidal zone’. (Fig. 12). Moreover, sediment availability plays a crucial role in this process, as it determines whether tidal signatures can be effectively recorded (Davis, 2012). Under low river discharge—when tidal oscillations have the greatest impact on river flow—tidal signatures are often poorly preserved due to limited sediment supply, both in bedload and suspended load (Fig. 12, first bar deposit). As discharge increases (Fig. 12, second bar deposit), more sediment is mobilized, enhancing the ability to record tidal signature at elevations that reflect the ‘average-discharge intertidal zone’. During major floods (Fig. 12, third bar deposit), a combination of high sediment supply and elevation of the water level and thereby intertidal zone, tidal modulation of riverine currents have the potential to become recorded at vertical positions higher than the ‘average-discharge intertidal zone’. However, this can only occur when the tidal modulation is not fully suppressed by the strong river discharge during peak discharge conditions. Additionally, deposited in this ‘elevated intertidal zone’ are subsequently protected from erosion until the next high-discharge event, and may therefore have a greater preservation potential. Therefore, varying discharge conditions influence not only the preservation potential of tidal signatures but also promote a vertical spread of tidal indicators within channelized deposits.

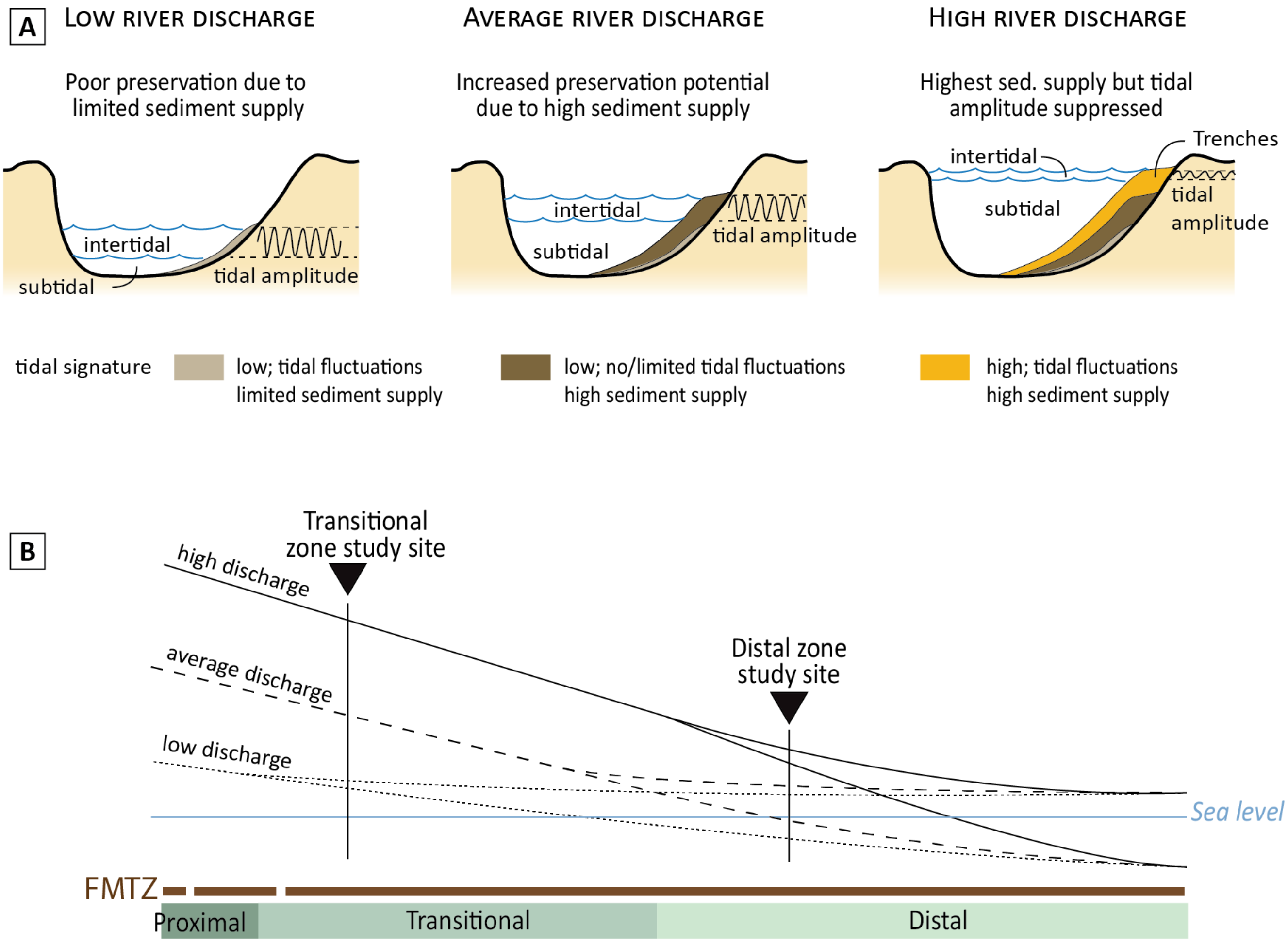

Fig 12. Dynamic intertidal zone. A) High river discharge elevates the intertidal zone and may allow the recording of tidal signals in the river flood deposits. Interplays between discharge, sediment supply and tidal range determine whether tidal sedimentary features could be recorded. Scenarios based on historical hydrographs, facies and cross-stratification analysis within the upstream part of the distal zone. B) The schematic longitudinal water-level profile is conceptual and depicts the different study sites for cross-stratification analysis in the distal and transitional zone, the proximal location is updip of the profile. Potential recording of tidal signals at other locations along the fluvial-marine transition zone would be speculative and is beyond the scope of this study.

5.4. Application and implications for interpreting ancient deposits in the FMTZ

The often under- or overestimated ability of tides to imprint the sedimentary record has important implications for interpreting ancient deposits, particularly when attempting to quantifying the impact of tidal processes on sedimentary dynamics.

Recent advances in understanding mixed energy systems highlight that the interplay of different processes can be cryptic to decipher (Gugliotta *et al.*, 2016b; Collins *et al.*, 2018; van Yperen *et al.*, 2020; Dashtgard *et al.*, 2021; Zuchuat *et al.*, 2023), and caution for the ‘overinterpretation’ of tidal energy in mixed systems where the river energy is dominant (Gugliotta *et al.*, 2023). For instance, the emphasis on tide-related sedimentary features in the well-studied Upper Cretaceous Sego Sandstone (USA) coastal to shallow-marine succession led to its interpretation as a system strongly influenced by tides (e.g. Wagoner, 1991; Willis & Gabel, 2001, 2003; van Cappelle *et al.*, 2016) whereas a recent study shows that, when considering all sedimentological, ichnological and stratigraphic observations together, the regional depositional context is better explained by a mixed-energy fluvial-dominated deltaic model (Gugliotta *et al.*, 2023). In studies of ancient deposits, reconstructing the role of tides in shaping depositional systems should not rely solely on sedimentary facies, but must be integrated with architectural analyses and paleocurrent data. In the Maastrichtian Tremp Formation (Tremp Basin, Spain), the limited presence of tidal signatures in sedimentary structures contrasts with palaeoecological evidence and the occurrence of marine microforaminiferal assemblages, which indicate landward-directed currents (Díez-Canseco *et al.*, 2014; Gómez-Gras *et al.*, 2016). In these deposits, the integration of architectural analysis with paleoflow patterns revealed the presence of a preserved tidal channel network (Ghinassi *et al.*, 2021), despite the cryptic nature of tidal signatures in terms of sedimentary structures. Alternatively, in subsurface studies using seismic attribute maps, assumptions about net/gross distributions and facies may be inferred from mapped planform geometries, which suggest the dominance of specific processes. However, the present study demonstrates that facies might be decoupled from morphological features. These observations highlight the importance of data integration and comprehensive 3D architectural and paleoflow analysis in interpreting ancient deltaic systems.

Interpretation of the tide-modulated bundles of the Po River also have significant implication sin interpretation of the rock record. In ancient strata, similar meter-scale bundling of cross strata is often interpreted to represent neap-spring cyclicity (e.g. Martinius & Gowland, 2011; Musial *et al.*, 2012; Abouessa *et al.*, 2014) and commonly mentioned as bundle sequence (Boersma, 1969; Visser, 1980). The meter-scale bundling observed in the Po River exhibits characteristics very similar to these ancient examples (Fig. 13), yet results from this work suggest deposition modulated by semi-diurnal tides acting over a timespan shorter than a full neap-spring cycle. Beyond exercising caution when interpreting bundles in cross-stratified deposits as tidal in origin (Reesink & Bridge, 2007, 2009), special care should be taken when associating them with neap–spring tidal cycles. If such an interpretation is based on sub-metric variations in cross-strata thickness, it should not only be supported by robust statistical analyses, but also consider whether the migration rate of the studied dune would reasonably have been on the order of just few centimeters per day (Martinius & Gowland, 2011) or less. Even after

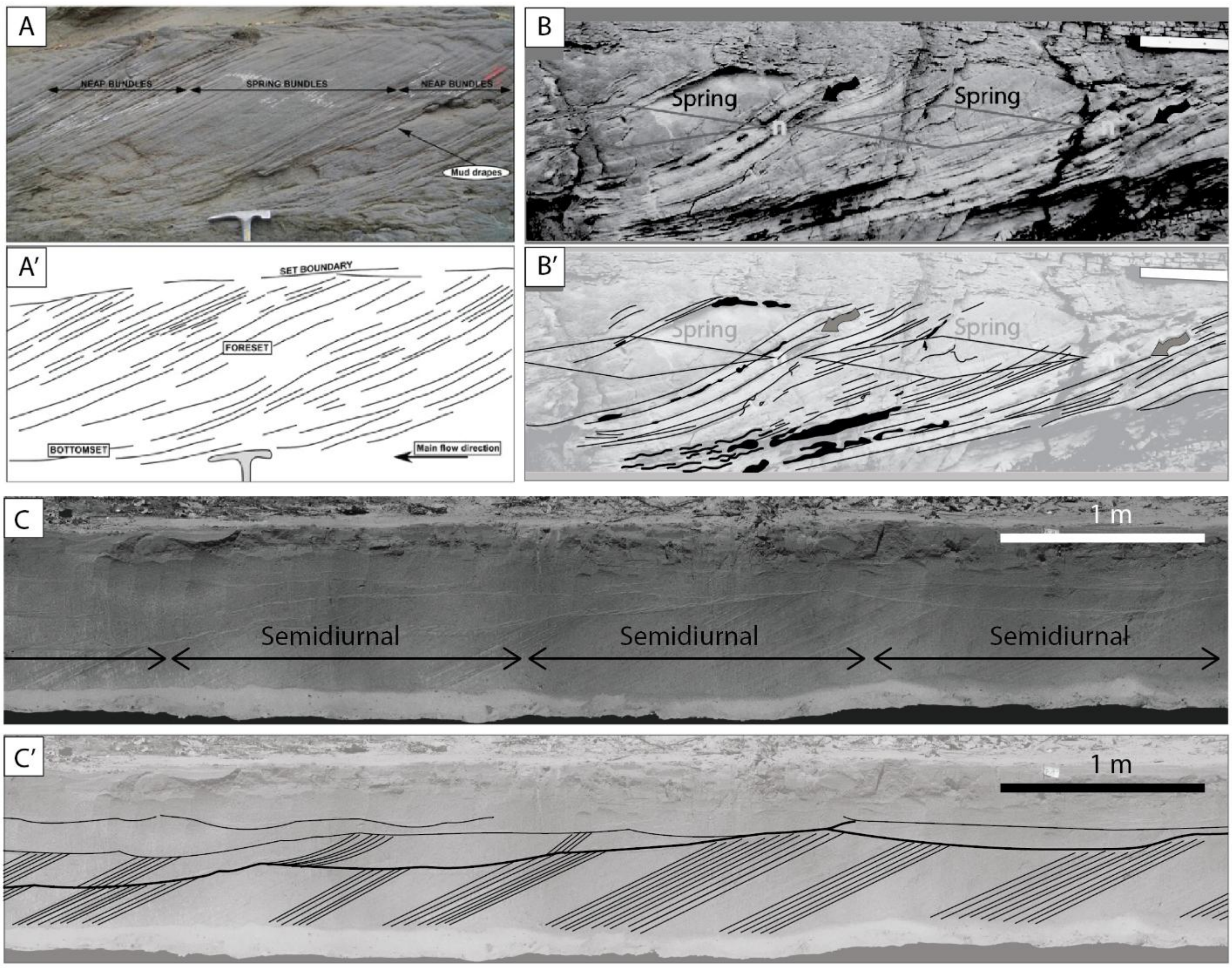

Fig. 13. Meter-scale cyclicity interpreted to represent neap-spring cyclicity in the A) McMurray Fm (Musial et al., 2012) and B) the Sabir Unit (Libya) (Abouessa et al., 2014). C) Meter-scale bundling in the Po River shows very similar characteristics but is interpreted to represent semi-diurnal tide-modulated deposition in a river-dominated setting.

establishing a tidal control on origin of bundles, bundle sequences should not be used to determine whether tidal processes were controlling or not morphodynamic processes. Similar caution applies to interpreting mud couplets, as there are currently no diagnostic criteria to reliably distinguish mud deposited during slack water in a purely tidal system from mud deposited under tidal modulation of riverine flow (e.g., during flood tides). Therefore, inferring the dominance of tidal processes based solely on the presence of specific sedimentary structures can be misleading.

6 Conclusions

In microtidal systems, tidal energy has a negligible influence on morphodynamic processes in comparison to fluvial or wave forces, and a limited occurrence of tidal signature (i.e. sedimentary structures) is commonly expected in deposits accumulated in these environments. This study documents the fingerprint of microtides on sediment deposition in river-dominated channels of the microtidal Po river-delta system, via integrated analysis of historical hydrographs, sedimentary facies along the distalmost 180 river kilometers. The most relevant insights of this study are summarized:

1) Tidal water level fluctuations occur as far as ~90 and ~40 river km updip during high and low discharge conditions, respectively. Tidal modulation occurs close to the river mouth also during the highest discharge events.

2) A tidal signature on deposits is common up to ~40 km from the river mouth, and is represented by equal and inequal double mud drapes, bidirectional current ripples and tide-modulated bundles in cross-stratified sand, despite the microtidal regime. The common assumption that deposits formed in microtidal environments rarely preserve tidal signatures should be reconsidered.

3) A dynamic zone prone to record tides is demonstrated based on tidal-modulated bundles preserved above the average intertidal zone. During low and high discharge events, the is zone is lowered and elevated, respectively, creating different degrees of tidal signature preservation potential, depending on the interplay of discharge, potential dampening of tidal water level fluctuations, and sediment

availability. Flood-enhanced water-level allowed tidal modulation to occur at elevated positions compared to the low-flow intertidal range.

4) The surprising ability of tides to leave distinctive sedimentary signatures even where they exert little geomorphic influence is counterintuitive and holds significant implications for the interpretation of ancient deposits. Tide-signed deposits are disproportional to tidal energy impacting fluvial processes.

5) Deposits with tidal indicators may be abundant despite the absence of a relevant control of tides on morpho-depositional processes. These results underscore the necessity to integrate sedimentological data with comprehensive 3D architectural and paleocurrent analysis for accurate paleoenvironmental reconstructions.

Acknowledgements

We thank Valentin Zuchuat, Marta Cosma, and Marcello Gugliotta for extensive discussions on the meaning of tidal indicators, Elena Bellizia for joining a field expedition and assisting with core preparation. Andrea D'Alpaos is thanked for valuable insights on the Po River hydrodynamics. Boatmen Michael and Natale and their extensive knowledge of the current Po River delta is beyond what literature can offer and exactly what we needed. The study was funded by AkerBP and undertaken as part of "The Geosciences for Sustainable Development" (CUP C93C23002690001).

Data availability

The data that support the findings of this study are available from the corresponding authors upon reasonable request.

References

Abouessa, A., **Duringer, P.**, **Schuster, M.**, **Pelletier, J.** and **Rubino, J.L.** (2014) Small-scale sedimentary structures and their implications in recognizing large-scale ancient tidal bedforms. Example from Dur At

Talah outcrop, Late Eocene, Sirt Basin, Libya. *J. African Earth Sci.*, **100**, 346–364.

Ainsworth, R.B., **Hasiotis, S.T.**, **Amos, K.J.**, **Krapf, C.B.E.**, **Payenberg, T.H.D.**, **Sandstrom, M.L.**, **Vakarelov, B.K.** and **Lang, S.C.** (2012) Tidal signatures in an intracratonic playa lake. Geology. doi: 10.1130/G32993.1

Archer, A.W. (2013) World's highest tides: Hypertidal coastal systems in North America, South America and Europe. *Sediment. Geol.*, **284**–**285**, 1–25.

Baas, J.H., **Best, J.L.** and **Peakall, J.** (2016) Predicting bedforms and primary current stratification in cohesive mixtures of mud and sand. *J. Geol. Soc. London.*, **173**, 12–45.

Best, J. and **Fielding, C.R.** (2019) Describing fluvial systems: linking processes to deposits and stratigraphy. *Geol. Soc. London, Spec. Publ.*, **488.1**, 152–166.

Bhattacharya, J.P. and **Giosan, L.** (2003) Wave-influenced deltas: Geomorphological implications for facies reconstruction. *Sedimentology*, **50**, 187–210.

Blum, M., **Martin, J.**, **Milliken, K.** and **Garvin, M.** (2013) Paleovalley systems: Insights from Quaternary analogs and experiments. *Earth-Science Rev.*, **116**, 128–169.

Boersma, J.R. (1969) Internal structure of some tidal mega-ripples on a shoal in the Westerschelde estuary, the Netherlands: report of a preliminary investigation.

Boldrin, A., **Langone, L.**, **Miserocchi, S.**, **Turchetto, M.** and **Acri, F.** (2005) Po River plume on the Adriatic continental shelf: Dispersion and sedimentation of dissolved and suspended matter during different river discharge rates. In: *Marine Geology*, 222–223,

Bradley, R.W. and **Venditti, J.G.** (2017) Reevaluating dune scaling relations. *Earth Sci. Rev.*, **165**, 356–376.

Broaddus, C.M., **Vulis, L.M.**, **Nienhuis, J.H.**, **Tejedor, A.**, **Brown, J.**, **Foufoula-Georgiou, E.** and **Edmonds, D.A.** (2022) First-order river delta morphology is explained by the sediment flux balance from rivers, waves, and tides. *Geophys. Res. Lett.*, **49**, e2022GL100355.

Cattaneo, A., **Correggiari, A.**, **Langone, L.** and **Trincardi, F.** (2003) The late-Holocene Gargano subaqueous delta, Adriatic shelf: Sediment pathways and supply fluctuations. *Mar. Geol.*, **193**, 61–91.

Cavaleri, L. (2000) The oceanographic tower Acqua Alta - activity and prediction of sea states at Venice. Coast Eng. doi: 10.1016/S0378-3839(99)00053-8

Choi, K. (2010) Rhythmic climbing-ripple cross-lamination in inclined heterolithic stratification (IHS) of a macrotidal estuarine channel, Gomso Bay, West Coast of Korea. *J. Sediment. Res.*, **80**, 550–561.

Choi, K. (2011) Tidal rhythmites in a mixed-energy, macrotidal estuarine channel, Gomso Bay, west coast of

Korea. *Mar. Geol.*, **280**, 105–115.

Choi, K., **Jo, J.** and **Kim, D.** (2021) Tidal and seasonal controls on the stratigraphic architecture of blind tidal channel deposits in the fluvial-tidal transition of the macrotidal Sittaung River estuary, Myanmar. Sediment Geol. doi: 10.1016/J.SEDGEO.2021.106029

Choi, K. and **Kim, D.H.** (2016) Morphologic and hydrodynamic controls on the occurrence of tidal bundles in an open-coast macrotidal environment, northern Gyeonggi Bay, west coast of Korea. *Sediment. Geol.*, **339**, 68–82.

Choi, K.S., **Dalrymple, R.W.**, **Chun, S.S.** and **Kim, S.P.** (2004) Sedimentology of modern, inclined heterolithic stratification (IHS) in the macrotidal Han River delta, Korea. J Sediment Res. doi: 10.1306/030804740677

Coleman, J.M. and **Gagliano, S.M.** (1960) Sedimentary structures: Mississippi deltaic plain. In: *Primary Sedimentary Structures and Their Hydrodynamic Interpretation*,

Collins, D.S., **Johnson, H.D.**, **Allison, P.A.** and **Damit, A.R.** (2018) Mixed process, humid-tropical, shoreline–shelf deposition and preservation: Middle Miocene–modern Baram Delta Province, Northwest Borneo. *J. Sediment. Res.*, **88**, 399–430.

Correggiari, A., **Cattaneo, A.** and **Trincardi, F.** (2005) The modern Po Delta system: Lobe switching and asymmetric prodelta growth. *Mar. Geol.*, **222**–**223**, 49–74.

Cosma, M., **Lague, D.**, **D'Alpaos, A.**, **Leroux, J.**, **Feldmann, B.** and **Ghinassi, M.** (2022) Sedimentology of a hypertidal point bar (Mont-Saint-Michel Bay, north-western France) revealed by combining lidar time-series and sedimentary core data. Sedimentology. doi: 10.1111/sed.12942

Dalrymple, R.W. and **Choi, K.** (2007) Morphologic and facies trends through the fluvial-marine transition in tide-dominated depositional systems: A schematic framework for environmental and sequence-stratigraphic interpretation. *Earth-Science Rev.*, **81**, 135–174.

Dalrymple, R.W., **Kurcinka, C.E.**, **Jablonski, B.V.J.**, **Ichaso, A.A.** and **Mackay, D.A.** (2015) Deciphering the relative importance of fluvial and tidal processes in the fluvial–marine transition. In: *Development in Sedimentology, Fluvial-Tidal Sedimentology* (Ed. P.J. Ashworth, J.L. Best, and D.R. Parsons), *Amsterdam, Elsevier*, 68, 3–40.

Dashtgard, S.E., **Vaucher, R.**, **Yang, B.** and **Dalrymple, R.W.** (2021) Hutchison Medallist 1. Wave-dominated to tide-dominated coastal systems: A unifying model for tidal shorefaces and refinement of the coastal-environments classification scheme. *Geosci. Canada*, **48**, 5–22.

Davide, V., **Pardos, M.**, **Diserens, J.**, **Ugazio, G.**, **Thomas, R.** and **Dominik, J.** (2003) Characterisation of bed sediments and suspension of the river Po (Italy) during normal and high flow conditions. *Water Res.*, **37**, 2847–2864.

Davis, R.A.D. (2012) Tidal signatures and their preservation potential in stratigraphic sequences. In: *Principles of Tidal Sedimentology* (Ed. R.W.D. Richard A. Davis Jr.), *Springer Netherlands*, Dordrecht, 35–55.

De Mowbray, T. and **Visser, M.J.** (1984) Reactivation surfaces in subtidal channel deposits, Oosterschelde, southwest Netherlands. J Sediment Petrol. doi: 10.1306/212F8503-2B24-11D7-8648000102C1865D

Díez-Canseco, D., **Arz, J.A.**, **Benito, M.I.**, **Díaz-Molina, M.** and **Arenillas, I.** (2014) Tidal influence in redbeds: A palaeoenvironmental and biochronostratigraphic reconstruction of the Lower Tremp Formation (South-Central Pyrenees, Spain) around the Cretaceous/Paleogene boundary. *Sediment. Geol.*, **312**, 31–49.

Dykstra, S.L., **Dzwonkowski, B.** and **Torres, R.** (2022) The role of river discharge and geometric structure on diurnal tidal dynamics, Alabama, USA. J Geophys Res Ocean. doi: 10.1029/2021JC018007

Fernandes, A.M., **Törnqvist, T.E.**, **Straub, K.M.** and **Mohrig, D.** (2016) Connecting the backwater hydraulics of coastal rivers to fluvio-deltaic sedimentology and stratigraphy. *Geology*, **44**, 979–982.

Ferrarin, C., **Maicu, F.** and **Umgiesser, G.** (2017) The effect of lagoons on Adriatic Sea tidal dynamics. *Ocean Model.*, **119**, 57–71.

Finotello, A., **D'Alpaos, A.**, **Bogoni, M.**, **Ghinassi, M.** and **Lanzoni, S.** (2020) Remotely-sensed planform morphologies reveal fluvial and tidal nature of meandering channels. *Sci. Rep.*, **10**, 1–13.

Galloway, W.E. (1975) Process framework for describing the morphological and stratigraphic evolution of deltaic depositional systems. In: *Deltas: Models for Exploration* (Ed. M.L. Broussard), *Houston Geological Society*, 87–98.

Ghinassi, M., **Oms, O.**, **Cosma, M.**, **Finotello, A.** and **Munari, G.** (2021) Reading tidal processes where their signature is cryptic: The Maastrichtian meandering channel deposits of the Tremp Formation (Southern Pyrenees, Spain). Sedimentology. doi: 10.1111/sed.12840

Godin, G. (1991) Frictional effects in river tides. In: *Tidal Hydrodynamics*, *John Wiley & Sons*, 379–402.

Gómez-Gras, D., **Roigé, M.**, **Fondevilla, V.**, **Oms, O.**, **Boya, S.** and **Remacha, E.** (2016) Provenance constraints on the Tremp Formation paleogeography (southern Pyrenees): Ebro Massif VS Pyrenees sources. *Cretac. Res.*, **57**, 414–427.

Goodbred, S.L. and **Saito, Y.** (2012) Tide-dominated deltas. *Princ. Tidal Sedimentol.*, **9789400701236**, 129–149.

Govi, M. and **Maraga, F.** (2005) Inundation on the Po Plain caused by levee breaches. *G. di Geol. Appl.*, 167–176.

Gugliotta, M., **Collins, D.S.**, **MacEachern, J.A.** and **El Euch-El Koundi, N.** (2023) Reevaluating the process regime in the Sego Sandstone: Sedimentological and ichnological evidence for an underemphasised fluvial signature. Depos Rec. doi: 10.1002/dep2.245

Gugliotta, M., **Flint, S.S.**, **Hodgson, D.M.** and **Veiga, G.D.** (2016a) Recognition criteria, characteristics and implications of the fluvial to marine transition zone in ancient deltaic deposits (Lajas Formation, Argentina). *Sedimentology*, **63**, 1971–2001.

Gugliotta, M., **Kurcinka, C.E.**, **Dalrymple, R.W.**, **Flint, S.S.** and **Hodgson, D.M.** (2016b) Decoupling seasonal fluctuations in fluvial discharge from the tidal signature in ancient deltaic deposits: an example from the Neuquén Basin, Argentina. *J. Geol. Soc. London.*, **173**, 94–107.

Gugliotta, M., **Saito, Y.**, **Nguyen, V.L.**, **Ta, T.K.O.**, **Nakashima, R.**, **Tamura, T.**, **Uehara, K.**, **Katsuki, K.** and **Yamamoto, S.** (2017) Process regime, salinity, morphological, and sedimentary trends along the fluvial to marine transition zone of the mixed-energy Mekong River delta, Vietnam. *Cont. Shelf Res.*, **147**, 7–26.

Gugliotta, M., **Saito, Y.**, **Nguyen, V.L.**, **Ta, T.K.O.**, **Tamura, T.** and **Fukuda, S.** (2018) Tide- and river-generated mud pebbles from the fluvial to marine transition zone of the Mekong River delta, Vietnam. J Sediment Res. doi: 10.2110/jsr.2018.54

Guo, L., **Zhu, C.**, **Wu, X.**, **Wan, Y.**, **Jay, D.A.**, **Townend, I.**, **Wang, Z.B.** and **He, Q.** (2020) Strong inland propagation of low-frequency long waves in river estuaries. Geophys Res Lett. doi: 10.1029/2020GL089112

Hendershot, M.L., **Venditti, J.G.**, **Bradley, R.W.**, **Kostaschuk, R.A.**, **Church, M.** and **Allison, M.A.** (2016) Response of low-angle dunes to variable flow. Sedimentology. doi: 10.1111/sed.12236

Herbert, C.M., **Alexander, J.**, **Amos, K.J.** and **Fielding, C.R.** (2020) Unit bar architecture in a highly-variable fluvial discharge regime: Examples from the Burdekin River, Australia. Sedimentology. doi: 10.1111/sed.12655

Hoitink, A.J.F. and **Jay, D.A.** (2016) Tidal river dynamics: Implications for deltas. *Rev. Geophys.* , **54**, 240–272.

Hughes, Z.J. (2011) Tidal channels on tidal flats and marshes. In: *Principles of Tidal Sedimentology* (Ed. R. Davis Jr. and R. Dalrymple), *Springer Netherlands*, Dordrecht, 269–300.

Jay, D.A. (1991) Green’s law revisited: Tidal long-wave propagation in channels with strong topography. *J.*

Geophys. Res. Ocean., **96**, 20585–20598.

Kästner, K., **Hoitink, A.J.F.**, **Torfs, P.J.J.F.**, **Deleersnijder, E.** and **Ningsih, N.S.** (2019) Propagation of tides along a river with a sloping bed. J Fluid Mech. doi: 10.1017/jfm.2019.331

Kirby, R. and **Parker, W.R.** (1982) A suspended sediment front in the Severn Estuary. Nature. doi: 10.1038/295396a0

Lanzoni, S. and **D'Alpaos, A.** (2015) On funneling of tidal channels. *J. Geophys. Res. Earth Surf.*, **120**, 433–452.

Lanzoni, S., **Luchi, R.** and **Bolla Pittaluga, M.** (2015) Modeling the morphodynamic equilibrium of an intermediate reach of the Po River (Italy). *Adv. Water Resour.*, **81**, 95–102.

Lefebvre, A. and **Cisneros, J.** (2023) The influence of dune lee side shape on time-averaged velocities and turbulence. *Earth Surf. Dyn.*, **11**, 575–591.

Leonardi, N., **Kolker, A.S.** and **Fagherazzi, S.** (2015) Interplay between river discharge and tides in a delta distributary. Adv Water Resour. doi: 10.1016/j.advwatres.2015.03.005

Li, S., **Li, S.**, **Shan, X.**, **Gong, C.** and **Yu, X.** (2017) Classification, formation, and transport mechanisms of mud clasts. Int Geol Rev. doi: 10.1080/00206814.2017.1287014

Longhitano, S.G., **Mellere, D.**, **Steel, R.J.** and **Ainsworth, R.B.** (2012) Tidal depositional systems in the rock record: A review and new insights. Sediment. Geol. 279:

Martin, A.J. (2000) Flaser and wavy bedding in ephemeral streams: a modern and an ancient example. *Sediment. Geol.*, **136**, 1–5.

Martinius, A.W. and **Gowland, S.** (2011) Tide-influenced fluvial bedforms and tidal bore deposits (Late Jurassic Lourinhã Formation, Lusitanian Basin, Western Portugal). *Sedimentology*, **58**, 285–324.

Maselli, V., **Normandeau, A.**, **Nones, M.**, **Tesi, T.**, **Langone, L.**, **Trincardi, F.** and **Bohacs, K.M.** (2020) Tidal modulation of river-flood deposits: How low can you go? *Geology*, **48**, 663–667.

Milligan, T.G., **Hill, P.S.** and **Law, B.A.** (2007) Flocculation and the loss of sediment from the Po River plume. *Cont. Shelf Res.*, **27**, 309–321.

Musial, G., **Reynaud, J.Y.**, **Gingras, M.K.**, **Féniès, H.**, **Labourdette, R.** and **Parize, O.** (2012) Subsurface and outcrop characterization of large tidally influenced point bars of the Cretaceous McMurray Formation (Alberta, Canada). Sediment Geol. doi: 10.1016/j.sedgeo.2011.04.020

Nelson, B.H. (1970) Hydrography, sediment dispersal, and recent historical development of the Po River delta, Italy. In: *Deltaic Sedimentation, Modern and Ancient*, Special Pu (Ed. J.P. Morgan), *Soc. Econ. Paleontol.*

Mineral, 152–184.

Nichols, M.M. and **Biggs, R.B.** (1985) Estuaries. In: *Coastal Sedimentary Environments* (Ed. R.A. Davis), *Springer New York*, New York, NY, 77–186.

Nienhuis, J.H., **Ashton, A.D.**, **Edmonds, D.A.**, **Hoitink, A.J.F.**, **Kettner, A.J.**, **Rowland, J.C.** and **Törnqvist, T.E.** (2020) Global-scale human impact on delta morphology has led to net land area gain. *Nature*, **577**, 514–518.

Nittrouer, J.A., **Mohrig, D.** and **Allison, M.** (2011a) Punctuated sand transport in the lowermost Mississippi River. *J. Geophys. Res. Earth Surf.*, **116**, 4025.

Nittrouer, J.A., **Mohrig, D.**, **Allison, M.A.** and **Peyret, A.P.B.** (2011b) The lowermost Mississippi River: A mixed bedrock-alluvial channel. Sedimentology. doi: 10.1111/j.1365-3091.2011.01245.x

Ohata, K., **Naruse, H.** and **Izumi, N.** (2022) Upper and lower plane bed definitions revised. Prog Earth Planet Sci. doi: 10.1186/s40645-022-00481-8

Orlić, M., **Kuzmić, M.** and **Pasarić, Z.** (1994) Response of the Adriatic Sea to the Bora and Sirocco forcing. Cont Shelf Res. doi: 10.1016/0278-4343(94)90007-8

Paniagua-Arroyave, J.F. and **Nienhuis, J.H.** (2024) The quantified Galloway ternary diagram of delta morphology. *J. Geophys. Res. Earth Surf.*, **129**, e2024JF007878.

Paola, C. and **Mohrig, D.** (1996) Palaeohydraulics revisited: palaeoslope estimation in coarse-grained braided rivers. *Basin Res.*, **8**, 243–254.

Patruno, S., **Hampson, G.J.** and **Jackson, C.A.L.** (2015) Quantitative characterisation of deltaic and subaqueous clinoforms. *Earth-Science Rev.*, **142**, 79–119.

Pomaro, A., **Cavaleri, L.**, **Papa, A.** and **Lionello, P.** (2018) 39 years of directional wave recorded data and relative problems, climatological implications and use. Sci Data. doi: 10.1038/sdata.2018.139

Ragno, N., **Tambroni, N.** and **Bolla Pittaluga, M.** (2020) Effect of small tidal fluctuations on the stability and equilibrium configurations of bifurcations. J Geophys Res Earth Surf. doi: 10.1029/2020JF005584

Reesink, A.J.H. and **Bridge, J.S.** (2007) Influence of superimposed bedforms and flow unsteadiness on formation of cross strata in dunes and unit bars. Sediment Geol. doi: 10.1016/j.sedgeo.2007.02.005

Reesink, A.J.H. and **Bridge, J.S.** (2009) Influence of bedform superimposition and flow unsteadiness on the formation of cross strata in dunes and unit bars - Part 2, further experiments. Sediment Geol. doi: 10.1016/j.sedgeo.2009.09.014

Reesink, A.J.H. and **Bridge, J.S.** (2011) Evidence of bedform superimposition and flow unsteadiness in unit-bar deposits, South Saskatchewan river, Canada. J Sediment Res. doi: 10.2110/jsr.2011.69

Roberts, H.H., **Walker, N.**, **Cunningham, R.**, **Kemp, G.P.** and **Majersky, S.** (1997) Evolution of sedimentary architecture and surface morphology: Atchafalaya and Wax Lake Deltas, Louisiana (1973-1994). *Gulf Coast Assoc. Geol. Soc. Trans.*, **47**, 477–484.

Rubin, D.M. and **Hunter, R.E.** (1982) Bedform climbing in theory and nature. Sedimentology. doi: 10.1111/j.1365-3091.1982.tb01714.x

Sassi, M.G., **Hoitink, A.J.F.**, **De Brye, B.**, **Vermeulen, B.** and **Deleersnijder, E.** (2011) Tidal impact on the division of river discharge over distributary channels in the Mahakam Delta. *Ocean Dyn.*, **61**, 2211–2228.

Savenije, H.H.G., **Toffolon, M.**, **Haas, J.** and **Veling, E.J.M.** (2008) Analytical description of tidal dynamics in convergent estuaries. *J. Geophys. Res. Ocean.*, **113**, 10025.

Sisulak, C.F. and **Dashtgard, S.E.** (2012) Seasonal controls on the development and character of inclined heterolithic stratification in a tide-influenced, fluvially dominated channel: Fraser River, Canada. *J. Sediment. Res.*, **82**, 244–257.

Szupiany, R.N., **Amsler, M.L.**, **Hernandez, J.**, **Parsons, D.R.**, **Best, J.L.**, **Fornari, E.** and **Trento, A.** (2012) Flow fields, bed shear stresses, and suspended bed sediment dynamics in bifurcations of a large river. Water Resour Res. doi: 10.1029/2011WR011677;PAGE:STRING:ARTICLE/CHAPTER

Tarolli, P., **Luo, J.**, **Straffelini, E.**, **Liou, Y.-A.**, **Nguyen, K.-A.**, **Laurenti, R.**, **Masin, R.** and **D'Agostino, V.** (2023) Saltwater intrusion and climate change impact on coastal agriculture. *PLOS Water*, **2**, e0000121.

Terwindt, J.H.T. (1981) Origin and Sequences of Sedimentary Structures in Inshore Mesotidal Deposits of the North Sea. In: *Holocene Marine Sedimentation in the North Sea Basin*,

Tessier, B. (1993) Upper intertidal rhythmites in the Mont-Saint-Michel Bay (NW France): Perspectives for paleoreconstruction. *Mar. Geol.*, **110**, 355–367.

Thomas, R.G., **Smith, D.G.**, **Wood, J.M.**, **Visser, J.**, **Calverley-Range, E.A.** and **Koster, E.H.** (1987) Inclined heterolithic stratification—Terminology, description, interpretation and significance. *Sediment. Geol.*, **53**, 123–179.

Trincardi, F., **Amorosi, A.**, **Bosman, A.**, **Correggiari, A.**, **Madricardo, F.** and **Pellegrini, C.** (2019) Ephemeral rollover points and clinothem evolution in the modern Po Delta based on repeated bathymetric surveys. *Basin Res.*, **32**, 402–418.

Trincardi, F., **Cattaneo, A.**, **Asioli, A.**, **Correggiari, A.** and **Langone, L.** (1996) Stratigraphy of the late-Quaternary deposits in the central Adriatic basin and the record of short-term climatic events. *Memorie-Istituto Ital. di Idrobiol.*, **55**, 39–70.

van Cappelle, M., **Stukins, S.**, **Hampson, G.J.** and **Johnson, H.D.** (2016) Fluvial to tidal transition in proximal, mixed tide-influenced and wave-influenced deltaic deposits: Cretaceous lower Sego Sandstone, Utah, USA. *Int. Assoc. Sedimentol. Spec. Publ.*, 1333–1361.

van den Berg, J.H., **Boersma, J.R.** and **van Gelder, A.** (2007) Diagnostic sedimentary structures of the fluvial-tidal transition zone; evidence from deposits of the Rhine and Meuse. *Netherlands J. Geosci. / Geol. en Mijnb.*, **86**, 287–306.

Van Yperen, A.E., **Holbrook, J.M.**, **Poyatos-Moré, M.** and **Midtkandal, I.** (2024) Backwater length estimates in modern and ancient fluvio-deltaic settings: Review and proposal of standardized workflows. Earth Sci Rev. doi: https://doi.org/10.1016/j.earscirev.2024.104692

van Yperen, A.E., **Poyatos-Moré, M.**, **Holbrook, J.M.** and **Midtkandal, I.** (2020) Internal mouth-bar variability and preservation of subordinate coastal processes in low-accommodation proximal deltaic settings (Cretaceous Dakota Group, New Mexico, USA). *Depos. Rec.*, **6**, 431–458.

Visentini, M. and **Borghi, G.** (1938) Le spiagge padane. Ricerche Sulle Sariazioni Delle Spiagge Italian. *CNR Report, Roma*, **7**, 137.

Visser, M.J. (1980) Neap- spring cycles reflected in Holocene subtidal large-scale bedform deposits: a preliminary note (Netherlands). Geology. doi: 10.1130/0091-7613(1980)8<543:NCRIHS>2.0.CO;2

Vulis, L., **Tejedor, A.**, **Ma, H.**, **Nienhuis, J.H.**, **Broaddus, C.M.**, **Brown, J.**, **Edmonds, D.A.**, **Rowland, J.C.** and **Foufoula-Georgiou, E.** (2023) River delta morphotypes emerge from multiscale characterization of shorelines. *Geophys. Res. Lett.*, **50**, e2022GL102684.

Wagoner, J.C. Van (1991) High-frequency sequence stratigraphy and facies architecture of the Sego Sandstone in the Book Cliffs of Western Colorado and Eastern Utah. In: *Sequence Stratigraphy Applications to Shelf Sandstone Reservoirs<subtitle>Outcrop to Subsurface Examples</subtitle>* (Ed. J.C. Van Wagoner, D. Nummedal, C.R. Jones, D.R. Taylor, D.C. Jenette, and G.W. Riley), *American Association of Petroleum Geologists*, Tulsa, OK,

Wang, Z.Y. and **Liang, Z.Y.** (2000) Dynamic characteristics of the Yellow River mouth. *Earth Surf. Process. Landforms*, **25**, 765–782.

Willis, B.J. and **Gabel, S.** (2001) Sharp-based, tide-dominated deltas of the Sego Sandstone, Book Cliffs, Utah, USA. *Sedimentology*, **48**, 479–506.

Willis, B.J. and **Gabel, S.L.** (2003) Formation of deep incisions into tide-dominated river deltas: Implications for the Stratigraphy of the Sego Sandstone, Book Cliffs, Utah, U.S.A. *J. Sediment. Res.*, **73**, 246–263.

Wright, S. and **Parker, G.** (2005) Modeling downstream fining in sand-bed rivers. I: Formulation. *J. Hydraul. Res.*, **43**, 613–620.

Yu, M., **Li, Y.**, **Zhang, K.**, **Yu, J.**, **Guo, X.**, **Guan, B.**, **Yang, J.**, **Zhou, D.**, **Wang, X.**, **Li, X.** and **Zhang, X.** (2023) Studies on the dynamic boundary of the fresh-salt water interaction zone of estuary wetland in the Yellow River Delta. Ecol Eng. doi: 10.1016/j.ecoleng.2023.106893

Zheng, S., **Edmonds, D.A.**, **Wu, B.** and **Han, S.** (2019) Backwater controls on the evolution and avulsion of the Qingshuigou channel on the Yellow River Delta. *Geomorphology*, **333**, 137–151.

Zuchuat, V., **Gugliotta, M.**, **Poyatos-Moré, M.**, **van der Vegt, H.**, **Collins, D.S.** and **Vaucher, R.** (2023) Mixed depositional processes in coastal to shelf environments: Towards acknowledging their complexity. Depos Rec. doi: 10.1002/dep2.229

Figure legends / captions

Fig. 1. A) Map of Italy and inset showing location of study area. B) Aerial picture of the studied Po River transect showing gauge locations (blue triangles) and extent of the FMTZ and backwater zone. C) Detailed aerial picture of the Po Delta plain, showing multiple distributary channels and beach barrier ridges, typical for strong influence of river and wave energy, respectively. No morpho-sedimentary features typical for tidal sedimentary processes are present, which is also visible in D) Historical map from 1811 (modified from Visentini & Borghi, 1938). E) Tidal forcing is mixed semidiurnal (data from http://idrometri.agenziapo.it/). F and G: aerial pictures (image©: Google, Landsat/Copernicus) highlighting the contrasting morphological characteristics of the Po River and Venice Lagoon, despite them being only ~70 km apart and experiencing the same tidal forcing.

Fig. 2. A) Longitudinal riverbed profile of the 180-km long studied Po River transect along the Pila distributary channel. Water elevation profiles for high and average discharge conditions are shown as well as the channel thalweg elevation. C-M) Water level fluctuations for selected periods representative for low, average, and high discharge conditions.

Fig. 3. Water level fluctuations for a short-lived high-discharge event. Vertical axes have same scales as in Figure 2 to allow for comparison. Note how tidal modulation is present in the distal zone (Cavanella) but completely damped in the transitional zone (Polesella).

Fig. 4. A) Studied Po River transect with location of data collection; vibracores, grain size samples, trenches for cross-stratification analysis and gauge stations providing historical water level records. Note the identified proximal, transitional and distal zones. B) Each grain-size sample location represents 5 samples taken from channel bars with a ~100-m spacing. Image©: Google, Landsat/Copernicus. C) Example of one of the trenches dug for cross-stratification analysis.

Fig. 5. Grain-size trend along the most downstream ~180 river kilometres of the Po River. Blue dots represent the median grain size fraction at sampled locations, the grey area represents the 10-90 percentile. Each dot represents the average of 5 samples taken from channel bars with a ~100-m spacing.

Fig. 6. Photographs of selected facies recovered from the distal zone. A) Location and logs of Vibracore 1 and 2. B) Ripple laminated sand with a gradational lower boundary. C) Mud-sand alternations with erosive basal boundary and transitional upper boundary into laminated mud. D) Dewatering and bioturbation features obliterating original heterolithic bedding. E) Mud clasts. F) Ripple-laminated

sand with critical to supercritical climbing angles. G) Upstream-directed ripple-cross laminate at the top of a sandy layer. H). Poorly-sorted medium to very fine plane-parallel laminated sand with mud drapes. I) Consecutive mud-sand couplets. J) Double mud drapes demonstrating a diurnal inequality of semidiurnal tides. K) Plane-parallel mud layers with a varying degree of laminae preservation.

Fig. 7. Photographs of selected facies recovered from the downstream side of a mid-channel river bar in the distal zone. A) Location of the five short cores. B) Seaward directed ripple-laminated and cross-stratified medium sand. C) Well-sorted ripple-laminated sand alternating with mud strata. D) Alternating sand-mud strata. E) Heterolithic bedding with mud clasts and upstream-directed ripple-laminae. F and H) Extrapolation of recovered core based on field on-site observations, highlighting upstream-directed ripple-scale cross laminae in the upper part of mud-rich cross strata. G) Distorted and bioturbated thinly bedded mud-sand alternations.

Fig. 8. A) Part of trench T1 from the distal zone, showing alternating dark-coloured bundles with well-defined strata (B) and light-coloured bundles with faint stratification (C).

Fig. 9. Cumulative grain size measurements in the proximal and distal zone show clearly an absence and presence of the clay fraction in the light-coloured and dark-coloured laminae, respectively.

Fig. 10. (two pages) Orthorectified models for selected trenches from the proximal (A, B), transitional (C, D) and distal (E-J) zone. K-M show close-ups of reactivation surfaces. Note the presence of a cyclic pattern in cross-stratification bundling in the distal zone (E-J), contrasting the lack thereof in the proximal zone (A-B).

Fig. 11: Continuous Wavelet Transform (CWT) analysis of selected trenches. For each trench, cross-set thickness is plotted against progressive along-trench distance (top panel). The wavelet Power Spectrum showing the spatial distribution of dominant wavelengths in the cross-set thickness signal; the cone of influence (COI) is indicated by the non-gray-shaded region (lower panel). Thick black contours mark the 95% confidence level relative to a red-noise background spectrum with the same lag-1 autocorrelation as the analyzed signal. For each trench, the Global Wavelet Spectrum (GWS) is displayed on the right-hand side; the dashed red line represents the 95% confidence interval."

Fig 12. Dynamic intertidal zone. A) High river discharge elevates the intertidal zone and may allow the recording of tidal signals in the river flood deposits. Interplays between discharge, sediment supply and tidal range determine whether tidal sedimentary features could be recorded. Scenarios based on historical hydrographs, facies and cross-stratification analysis within the upstream part of the distal zone. B) The schematic longitudinal water-level profile is conceptual and depicts the different study sites for cross-stratification analysis in the distal and transitional zone, the proximal location is updip of the profile. Potential recording of tidal signals at other locations along the fluvial-marine transition zone would be speculative and is beyond the scope of this study.

Fig. 13. Meter-scale cyclicity interpreted to represent neap-spring cyclicity in the A) McMurray Fm (Musial *et al.*, 2012) and B) the Sabir Unit (Libya) (Abouessa *et al.*, 2014). C) Meter-scale bundling in the Po River shows very similar characteristics but is interpreted to represent semi-diurnal tide-modulated deposition in a river-dominated setting.

Table 1. Estimated flow depth based on the empirical scaling relationship between dune height and formative flow depth from Bradley & Venditti (2017). The stage needed for bedform deposition results from the waterdepth at gauge station needed to deposit the bedform and its relation discharge values computed / introduced in chapter 2.3. Formative depth was not reconstructed for unit bars, since they do not scale with water depth (in Herbert *et al.*, 2020).

Table 2. Key characteristics of the river-delta systems discussed in Section 6.1, relevant for comparing upstream tidal propagation. Data sourced from (Boldrin *et al.*, 2005; Nittrouer *et al.*, 2011a; Zheng *et al.*, 2019; Yu *et al.*, 2023).

Appendix

Fig. A) (next two pages). Results of laminae counting for all trenches. Note the clear bundling in the distal zone whereas this is absent in the proximal and transitional zones. The vertical axis scale is different for trenches in the distal zone. Additionally, the horizontal axis for Long Island 2 (distal zone) is different too.